

# Chapter 4

## The HXDS Solid State Detectors

*Walter C. McDermott, Shaun Serej, and Edwin M. Kellogg*

### 4.1 Introduction

This chapter describes the calibration of the HXDS Solid State Detectors (SSD) used during the ground calibration of AXAF. One SSD, `ssd_5`, was used as a Beam Normalization Detector in the Building 500 location, while the other, `ssd_x`, was used in the focal plane to measure the HRMA point response function and the HRMA effective area. This chapter is in a rather preliminary state, and all data contained in it should be accepted with caution.

### 4.2 Calibration Overview

The SSD's were calibrated using monochromatic and undispersed synchrotron radiation from the Physikalisch-Technische Bundesanstalt (PTB) beam lines, the SX700, a grating monochromator and the 12.20 or white beam line, an undispersed beam with no intervening optical elements between the beam source and the detector, and one BESSY beam line, the KMC or Krystall Monokromator, at the BESSY electron storage ring in Berlin, Germany. The calibration program is based on one designed earlier at PTB for use with lithium drifted silicon solid state detectors (Scholze and Ulm, 1994). First, we obtain pulse height distributions from the Ge detector at the SX700, from 0.4 to 1.7 keV, to derive the QE in narrow energy bands, as well as the pulse height distribution for a single energy (spectral response function, or SRF). The SX700 output beam is calibrated using the PTB electrical substitution cryogenic radiometer (Lederer et al., 1995), which is capable of 1% flux accuracy. The SX700 energy scale is calibrated to 2 eV, which also helps us to establish our SSD detectors' energy scales. This SX700 measurement is especially important below 1.6 keV because of the narrow absorption features and EXAFS in the SSD QE near the Al-K edge, 1.58 keV, Ge-L at 1.2 keV, and O-K at 0.54 keV.

At higher energies, the KMC was used to obtain the SRF, from 1.7 to 5.9 keV. It was not, however, possible to use the electrical substitution cryogenic radiometer with the KMC. In order to extend the QE calibration to higher energies, beyond the 1.7 keV upper limit of the SX700, we rely on the undispersed, or white, synchrotron beam, whose intensity can be calculated using PTB's measurements of the synchrotron ring current, beam energy, magnetic field, source-to-detector distance, beam emissivity, and detector aperture dimensions. The SRF measured with monochromatic

radiation is then convolved with the calculated synchrotron spectrum, and compared with the measured detector pulse height distribution. The comparison also accounts for the x-ray absorption taking place in the detector windows: the Al and parylene windows, and the inevitable layer of ice resulting from condensation of moisture on the cooled detector surface. The difference between predicted and observed pulse height distribution tells us the detector efficiency, since the intensity of the white beam from the synchrotron is calculated independently. While there is considerable room for uncertainty in this comparison at lower energies, where x-ray absorption in the detector windows is strong, at higher energies the windows are less important, and we are confronting the intrinsic absorption QE of the Ge detector crystal. We have always believed that this approaches 100%, but have set out to verify it for these detectors with the white beam calibration.

### 4.3 Spectral Response Function, SRF

The SRF is a description of how the detector redistributes a single-energy photon in pulse-height space. It was measured for the SSDs using monochromatic radiation from a double crystal monochromator on the BESSY KMC beam line at higher energies, and the PTB SX700 grating monochromator beam line at lower energies (Scholze and Ulm, 1994).

The KMC beam line was equipped with three selectable crystal sets: beryl, for the energy range between 800 eV and 1.7 keV, InSb for the energy range from 1.7 keV to 5.9 keV, and silicon for the range from 2.0 keV to 5.9 keV. Due to optics in the beam line and the characteristic operating conditions of the storage ring, the energies available from the KMC beam line were limited to less than or equal to 5.9 keV. The majority of the response function measurements were taken with the silicon crystal because the efficiency of the silicon monochromator over the needed energy range was relatively flat as opposed to the InSb crystal, whose efficiency is strongly dependent on energy. The InSb crystals were used mainly to bridge the gap between the beryl and Si crystals.

The SX700 beam line's energy range is from 70 eV to 1.7 keV. However, data were collected only down to 400 eV because the thermal noise in the SSD interferes with the x-ray peak below this energy. The SX700 had the added advantage that its absolute flux was calibrated using the electrical substitution cryogenic radiometer as a primary standard, and a set of photodiodes as transfer standards. This is discussed in the next section.

The SRF was generally measured in steps of 200 eV, but the step size was much finer through detector absorption features. This allows fitting the fine structure of these features.

#### 4.3.1 Components of the Response Function

Some of the response function spectra have been fit using the XSPEC (Arnaud, 1996) model `JMKmod` (Tsiang, 1997). This model is a subroutine in XSPEC that contains a modified version of the HYPERMET function (Phillips and Marlow (1976), Scholze and Ulm (1994)). The HYPERMET function is an empirical model that is commonly used to fit solid state detector spectra. This function is a sum of terms that model certain portions of the recorded spectrum. The following four components are included in `JMKmod`.

$$G(E) = H_G \exp \left[ -\frac{(E - E_0)^2}{2\sigma^2} \right] \quad (4.1)$$

$$T_L(E) = \frac{1}{2} H_{TL} \exp \left( \frac{E - E_0}{\beta_L} \right) \operatorname{erfc} \left( \frac{E - E_0}{\sqrt{2}\sigma} + \frac{\sqrt{2}\sigma}{2\beta_L} \right) \quad (4.2)$$

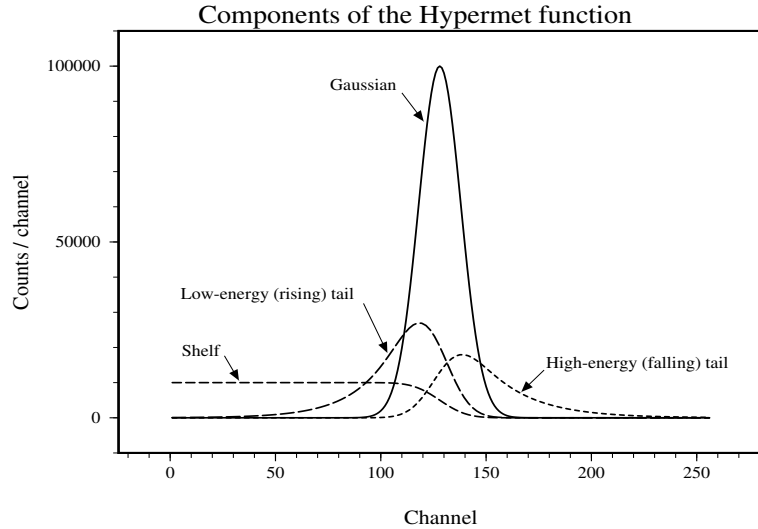


Figure 4.1: Components of the HYPERMET function.

$$T_P(E) = \frac{1}{2} H_{TP} \exp\left(\frac{E_0 - E}{\beta_P}\right) \operatorname{erfc}\left(\frac{E_0 - E}{\sqrt{2}\sigma} + \frac{\sqrt{2}\sigma}{2\beta_P}\right) \quad (4.3)$$

$$S(E) = \frac{1}{2} H_S \operatorname{erfc}\left(\frac{E - E_0}{\sqrt{2}\sigma}\right) \quad (4.4)$$

where  $G(E)$  is a Gaussian with  $H_G$ ,  $\sigma$ , and  $E_0$  as its amplitude, standard deviation, and center parameters, respectively, representing the main peak;  $T_L(E)$  is a low energy tail with amplitude and slope parameters of  $H_{TL}$  and  $\beta_L$ , respectively;  $T_P(E)$  is a high energy tail with  $H_{TP}$  and  $\beta_P$  as its amplitude and slope parameters; and  $S(E)$  is a stepwise flat shelf of amplitude  $H_S$ . A plot of the above four components is shown in Figure 4.1.

The Gaussian portion of the HYPERMET function is just the main line peak of the spectrum. This results from the conversion of all of the energy of a given photon into a pulse that is then recorded by the pulse-height analysis (PHA) chain. In an ideal detector, all of the photons from a monochromatic source would appear in the main peak. The width of this peak is influenced by the following factors: (1) the statistical spread in the number of electrons created by a given energy photon, and (2) fluctuations in the number of leakage current electrons across the detector diode, as well as (3) noise electrons in the FET preamp front end. The first contribution which is termed as the Fano broadening,  $\sigma_f$ , is expressed by

$$\sigma_f = (F \cdot E_0 \cdot W)^{1/2} \quad (4.5)$$

where  $W$  is the average energy required to create a free electron-hole pair in the detector material ( $\approx 3$  eV for germanium),  $E_0$  is the photon energy (peak center), and  $F$  is the Fano factor which

accounts for constrained limits on the number of electron-hole pairs that can be created. The last two contributions make up the electronic broadening,  $\sigma_e$ , which is energy independent. The full width of the peak at one-half of the maximum height is

$$FWHM = 2.355 (\sigma_f^2 + \sigma_e^2)^{1/2}. \quad (4.6)$$

The low energy tail represents the contributions of three effects: (1) incomplete charge collection in the detector due to recombination of charges and impurities that act as traps, (2) the escape of photoelectrons from the sensitive region near the surface, and (3) pulse pileup resulting from an “undershoot” condition of the amplifier pulses in the PHA chain. Each of these is described by an exponentially decaying distribution below the peak. The contributions of the first and second effects are similar since both cause incomplete charge collection. However, since the energy distribution of the photoelectrons that escape the surface is wider than those that are trapped or recombined in the active region, the contribution due to the second effect decays slower than that for the first effect. The third effect is count-rate dependent and occurs when the amplifier is over-damped so that after a pulse is processed, the amplifier baseline quickly restores itself to a level less than zero. A subsequent pulse rides on the tail of the first pulse. The output of the second is then lowered by the amount of the undershoot. The pulse is then placed in a bin in the multichannel analyzer that is lower in pulse height. Because the likelihood of a second pulse arriving during the undershoot increases with x-ray rate, the fraction of total counts in such a feature would increase with rate.

The high energy tail represents the pulse pileup resulting from an “overshoot” condition of the amplifier pulses. The overshoot occurs when the pole-zero cancellation in the amplifier is overcompensated, and thus the pulses do not return to the base line but overshoot. Consequently, when two pulses are close in time, one sits on the overshooting tail of the other and registers an amplitude in the multichannel analyzer that has a higher value than the true amplitude. This tail is described by an exponential function decaying above the peak (the so called “falling” tail).

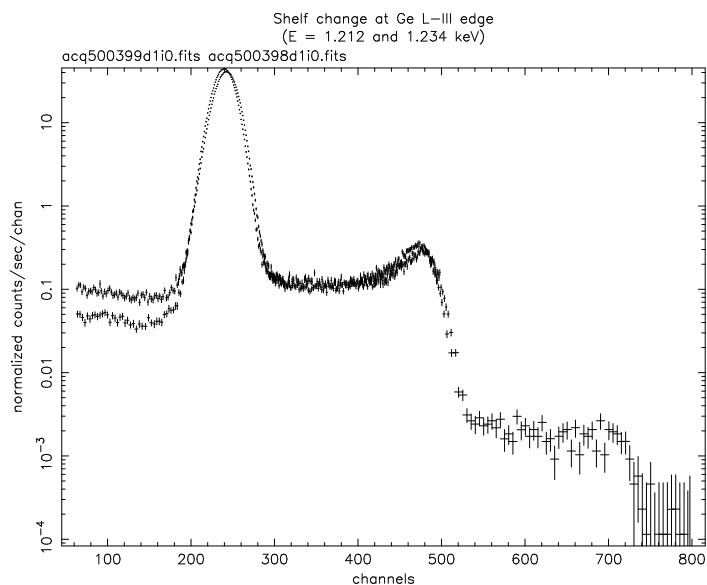
The pulse pileup for both undershoot and overshoot conditions, which is also called “tail pileup,” would tend to be suppressed by the action of pileup rejection circuitry, which was used in our apparatus. However, we discovered that the pileup rejection did not function properly below about 2 keV, so pulse pileup is significant at those low energies. But, since the pole-zero cancellation circuitry was disabled on the amplifiers in our apparatus, the overshoot condition was not expected to be present in our measurements.

The flat shelf is due to energy losses resulting from the transmission of primary (photo- and Auger) electrons in the detector dead layer, contacts, and any other filters outside the detector active area (Scholze and Ulm, 1994). The photo- and Auger electrons produced by the photon interactions within these layers lose energy or escape the detector as they travel towards the detector active region. The result is a pulse-height lower than would normally be expected. This shelf extends from the main peak down to zero pulse height, and is not rate-dependent.

In the JMKmod software (Tsiang, 1997), the HYPERMET model described above is formulated in the Fourier space, where the Gaussian distribution is represented by a moment generating function, and the tail and shelf components are generated by the convolution of this moment generating function with an exponential function.

Plots of some of the response functions are shown in Figures 4.2 and 4.3. The first figure is a plot of the change in the response function across the Ge  $L_{III}$  edge. As can be seen, the shelf increases as the energy goes above the absorption edge. This is because more photons are being absorbed relatively close to the surface of the crystal and do not have a chance for the full charge to migrate into the active region.

The plots in Figure 4.3 show the spectral response functions of *ssd\_5* and *ssd\_x* detectors at 4.1 keV. These spectra, in addition to the prominent features of the main peak (a Gaussian, a

Figure 4.2: Response functions of ssd.5 on both sides of the Ge L<sub>III</sub> edge.

low-energy tail, and shelf), display secondary features, such as, pileup, escape, and fluorescent peaks.

The escape peak is due to the escape of Ge-L x-rays from the detector. Ge-L and Al-K fluorescent peaks originate from the detector crystal material and the aluminum contact and filter material in the detector. The Si-K fluorescence is attributed to the Si crystals in the monochromator. The fluorescent peaks are located at fixed line energies in the spectrum, while the escape peak is always at a fixed separation below the main line peak energy.

Another aspect of the spectra is the smaller peak at twice the pulse height of the main peak. This peak can be a pileup peak, a second order photon peak from the monochromator, or a combination of both. When the energy for the monochromator is set above 2.9 keV, this smaller peak is all pileup because the optics in the beam line prohibit photons of energy beyond 5.9 keV from being introduced. The effects of pileup (rate-dependent) can also be separated from higher-order diffraction (rate-independent) by collecting spectra at different rates. Although the pileup rejection circuitry effectively eliminates pileup above 2 keV for count rates below 1000 Hz, it is unable to detect and reject the pileup events recorded at twice the pulse height of the main peak. Such pileup events involve pulses so close in time that cannot be detected by the pileup rejection circuit.

#### 4.3.2 Interpeak Pileup

Another feature in the measured response function, as shown in Figure 4.3, is the events that occur between the main peak and the second order peak. These events arise from a pileup situation where the pileup rejection circuitry in the amplifier does not work correctly. We have called these events interpeak pileup.

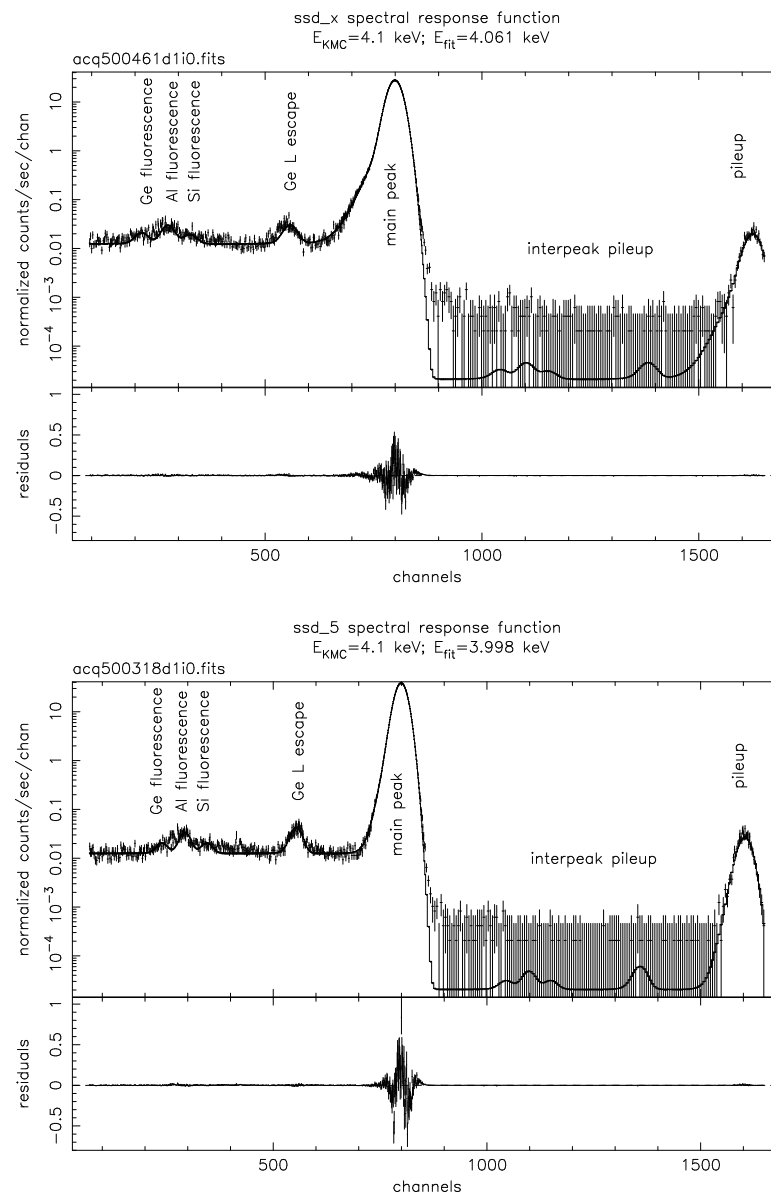


Figure 4.3: Response functions of ssd\_x and ssd.5 at 4.1 keV.

The amplifier has two branches to it. The first is a fast discriminator circuit that determines whether there are piled up events. The second is the processing branch which amplifies and shapes the pulse from the pre-amplifier. The fast discriminator looks at the time difference between two pulses. If they are deemed to be too close in time such that the tail of one pulse might influence the height of another, this circuit sends a veto signal to the multichannel analyzer telling it not to count the forthcoming pulses. The method in which this circuit determines the temporal separation of two pulses is to use one pulse to turn on a clock, known as an inspection interval, and look for a second pulse to arrive while this clock is active. In order to activate the inspection interval, the pulse must be above a threshold voltage determined by the local amplifier noise. If the pulse is below this threshold, it can pass through the amplifier without triggering the inspection circuit. This allows pileup to occur. This pileup is not limited to the normal “twice-the-pulse-height” pileup that happens when the two pulses are so close in time that the rejection circuit cannot resolve them, but can fall anywhere from twice the pulse height down to the height of the largest pulse. For the HXDS SSDs, this situation occurs at energies below about 2 keV (40 mV preamplifier output). Analysis of such spectra is more complicated, and causes uncertainties.

#### 4.4 Results of Fitting Response Function Spectra

The fitted response function includes a Gaussian, a low-energy tail, and a shelf component for the main line peak, as well as the same components for the escape and fluorescent lines. A sample of the XSPEC fits is shown in Figure 4.3. The high-energy tail component of the Hypermet function was not included in the fitted response function. Inclusion of such a tail improved the quality of the fits. However, the resulting values for the parameters of the tail suggested a tail pileup level as high as 20%, which is not possible for our 1000 Hz counting rate and 10  $\mu$ s amplifier shaping time. Further, since the pole-zero cancellation circuit in our amplifiers was disabled, no significant overshoot condition for the amplifier pulse tails could be expected. (An amplifier without the pole-zero cancellation is usually over-damped, i.e., pulse tails undershoot.) The small amount of high energy tailing that can be seen in the pulse height spectra shown in Figure 4.3 is attributed to the interpeak pileup, which was not included in the fitted response function model. In our recorded spectra, the interpeak pileup was less than 0.2% for energies higher than 2 keV. However, for lower energies, it increased to values as high as 4% as the energy approached 0.4 keV and the pileup rejection circuitry became increasingly less effective.

The fitted response function parameters for both `ssd_5` and `ssd_x` detectors in the energy range 0.4-5.9 keV are listed in Tables 4.1 – 4.4. The parameters for the energy range 0.4-1.7 keV are from fitting the spectra recorded at the SX700 beamline using a grating monochromator, and the parameters for the energy range 2.1-5.9 keV are from the spectra recorded at the KMC beamline using a silicon double crystal monochromator. Each row in the aforementioned tables shows the fitted parameters for a measured response function spectrum at a given x-ray energy, as identified by a “runid” and the monochromator energy setting  $E_{MC}$ . The listed parameters in these tables are:  $E_{fit}$ , the fitted line energy; t2norm, norm (area) of the low-energy tail; t2par, slope parameter of the low-energy tail; shelfnm, norm of the shelf; L2norm, norm of the Ge-L escape line; L3norm, norm of the Al-K fluorescent line; L4norm, norm of the Ge-L fluorescent line; and L5norm, norm of the Si-K fluorescent line. The tail and shelf norms are relative to the norm of the Gaussian component of the main line, and the escape and fluorescent line norms are relative to the norm of the main line (the sum of Gaussian, tail, and shelf norms).

The detector resolution parameters, the Fano factor and the electronic broadening (in channels), are shown in Table 4.5. As the value of these parameters show the `ssd_5` has a better spectral

runid	$E_{MC}$	$E_{fit}$ (keV)	t2norm	t2par	shelfnm
500504	0.400	0.404 ± 0.0000	4.0000 ± 0.0000	1.1400 ± 0.0000	0.0000 ± 0.0000
500508	0.450	0.454 ± 0.0000	4.0000 ± 0.0000	1.1040 ± 0.0000	0.0000 ± 0.0000
500510	0.500	0.505 ± 0.0000	4.0000 ± 0.0000	1.1230 ± 0.0044	0.0000 ± 0.0000
500505	0.538	0.538 ± 0.0000	4.0000 ± 0.0000	1.0940 ± 0.0026	0.0000 ± 0.0000
500507	0.548	0.555 ± 0.0000	4.0000 ± 0.0000	1.1060 ± 0.0016	0.0000 ± 0.0000
500509	0.600	0.610 ± 0.0000	4.0000 ± 0.0000	1.1020 ± 0.0009	0.0000 ± 0.0000
500511	0.700	0.705 ± 0.0000	1.0110 ± 0.1488	1.0940 ± 0.0035	0.0457 ± 0.0076
500512	0.800	0.803 ± 0.0000	0.4627 ± 0.0298	1.0780 ± 0.0018	0.0233 ± 0.0013
500513	0.900	0.902 ± 0.0000	0.3135 ± 0.0153	1.0710 ± 0.0013	0.0168 ± 0.0006
500524	1.000	1.000 ± 0.0000	0.2401 ± 0.0110	1.0670 ± 0.0012	0.0135 ± 0.0004
500523	1.100	1.100 ± 0.0000	0.1876 ± 0.0077	1.0610 ± 0.0010	0.0105 ± 0.0003
500522	1.200	1.200 ± 0.0000	0.1739 ± 0.0072	1.0610 ± 0.0010	0.0104 ± 0.0002
500521	1.212	1.212 ± 0.0000	0.1664 ± 0.0063	1.0580 ± 0.0009	0.0102 ± 0.0002
500520	1.234	1.231 ± 0.0000	0.7352 ± 0.0231	1.0600 ± 0.0005	0.0315 ± 0.0007
500519	1.300	1.300 ± 0.0000	2.5620 ± 0.1739	1.0570 ± 0.0003	0.1014 ± 0.0053
500518	1.400	1.400 ± 0.0000	1.9740 ± 0.0959	1.0520 ± 0.0003	0.0862 ± 0.0031
500514	1.500	1.503 ± 0.0000	1.9660 ± 0.0736	1.0480 ± 0.0002	0.0906 ± 0.0026
500545	1.555	1.555 ± 0.0000	1.7530 ± 0.0592	1.0480 ± 0.0002	0.0816 ± 0.0021
500548	1.560	1.559 ± 0.0000	1.6530 ± 0.0532	1.0480 ± 0.0002	0.0834 ± 0.0020
500541	1.570	1.571 ± 0.0000	1.9560 ± 0.0834	1.0480 ± 0.0002	0.1443 ± 0.0045
500540	1.575	1.575 ± 0.0000	1.7110 ± 0.0631	1.0480 ± 0.0002	0.1292 ± 0.0035
500539	1.580	1.581 ± 0.0000	1.8940 ± 0.0720	1.0480 ± 0.0002	0.1287 ± 0.0036
500537	1.590	1.590 ± 0.0000	1.6100 ± 0.0507	1.0480 ± 0.0002	0.1046 ± 0.0024
500533	1.600	1.602 ± 0.0000	1.8160 ± 0.0648	1.0480 ± 0.0002	0.1270 ± 0.0034
500534	1.605	1.606 ± 0.0000	1.6150 ± 0.0514	1.0470 ± 0.0002	0.1133 ± 0.0026
500535	1.610	1.610 ± 0.0000	1.5530 ± 0.0481	1.0470 ± 0.0002	0.1097 ± 0.0025
500536	1.630	1.629 ± 0.0000	1.4050 ± 0.0389	1.0460 ± 0.0002	0.0974 ± 0.0020
500544	1.650	1.648 ± 0.0000	1.3230 ± 0.0364	1.0460 ± 0.0002	0.0973 ± 0.0019
500530	1.700	1.698 ± 0.0000	1.1270 ± 0.0267	1.0440 ± 0.0002	0.0866 ± 0.0015
500231	2.100	2.132 ± 0.0000	0.6339 ± 0.0162	1.0390 ± 0.0002	0.0344 ± 0.0009
500233	2.300	2.323 ± 0.0000	0.5092 ± 0.0123	1.0390 ± 0.0002	0.0315 ± 0.0007
500239	2.500	2.516 ± 0.0000	0.3965 ± 0.0076	1.0370 ± 0.0002	0.0226 ± 0.0004
500235	2.700	2.708 ± 0.0000	0.3230 ± 0.0060	1.0360 ± 0.0002	0.0217 ± 0.0004
500238	2.900	2.902 ± 0.0000	0.2599 ± 0.0046	1.0340 ± 0.0002	0.0179 ± 0.0003
500240	3.100	3.095 ± 0.0000	0.2180 ± 0.0038	1.0330 ± 0.0002	0.0153 ± 0.0003
500241	3.300	3.289 ± 0.0000	0.1825 ± 0.0030	1.0320 ± 0.0002	0.0147 ± 0.0002
500242	3.500	3.483 ± 0.0000	0.1598 ± 0.0026	1.0310 ± 0.0002	0.0132 ± 0.0002
500243	3.700	3.676 ± 0.0000	0.1379 ± 0.0023	1.0300 ± 0.0002	0.0116 ± 0.0002
500244	3.900	3.869 ± 0.0000	0.1191 ± 0.0020	1.0290 ± 0.0002	0.0106 ± 0.0002
500245	4.100	4.063 ± 0.0000	0.1124 ± 0.0019	1.0290 ± 0.0002	0.0100 ± 0.0002
500247	4.300	4.256 ± 0.0000	0.0977 ± 0.0017	1.0280 ± 0.0002	0.0095 ± 0.0002
500249	4.700	4.640 ± 0.0000	0.0789 ± 0.0015	1.0280 ± 0.0002	0.0087 ± 0.0002
500250	5.100	5.026 ± 0.0000	0.0636 ± 0.0013	1.0270 ± 0.0003	0.0074 ± 0.0001
500251	5.500	5.410 ± 0.0000	0.0516 ± 0.0011	1.0260 ± 0.0003	0.0067 ± 0.0001
500252	5.900	5.786 ± 0.0000	0.0447 ± 0.0010	1.0260 ± 0.0003	0.0061 ± 0.0001

Table 4.1: Fitted energy, rising (low-energy) tail and shelf parameters for `ssd_x`.

runid	$E_{MC}$	L2norm	L3norm	L4norm	L5norm
500504	0.400	0.0000 ± 0.0000	0.0000 ± 0.0000	0.0000 ± 0.0000	0.0000 ± 0.0000
500508	0.450	0.0000 ± 0.0000	0.0000 ± 0.0000	0.0000 ± 0.0000	0.0000 ± 0.0000
500510	0.500	0.0000 ± 0.0000	0.0000 ± 0.0000	0.0000 ± 0.0000	0.0000 ± 0.0000
500505	0.538	0.0000 ± 0.0000	0.0000 ± 0.0000	0.0000 ± 0.0000	0.0000 ± 0.0000
500507	0.548	0.0000 ± 0.0000	0.0000 ± 0.0000	0.0000 ± 0.0000	0.0000 ± 0.0000
500509	0.600	0.0000 ± 0.0000	0.0000 ± 0.0000	0.0000 ± 0.0000	0.0000 ± 0.0000
500511	0.700	0.0000 ± 0.0000	0.0000 ± 0.0000	0.0000 ± 0.0000	0.0000 ± 0.0000
500512	0.800	0.0000 ± 0.0000	0.0000 ± 0.0000	0.0000 ± 0.0000	0.0000 ± 0.0000
500513	0.900	0.0000 ± 0.0000	0.0000 ± 0.0000	0.0000 ± 0.0000	0.0000 ± 0.0000
500524	1.000	0.0000 ± 0.0000	0.0000 ± 0.0000	0.0000 ± 0.0000	0.0000 ± 0.0000
500523	1.100	0.0000 ± 0.0000	0.0000 ± 0.0000	0.0000 ± 0.0000	0.0000 ± 0.0000
500522	1.200	0.0000 ± 0.0000	0.0000 ± 0.0000	0.0000 ± 0.0000	0.0000 ± 0.0000
500521	1.212	0.0000 ± 0.0000	0.0000 ± 0.0000	0.0000 ± 0.0000	0.0000 ± 0.0000
500520	1.234	0.0000 ± 0.0000	0.0000 ± 0.0000	0.0000 ± 0.0000	0.0000 ± 0.0000
500519	1.300	0.0000 ± 0.0000	0.0000 ± 0.0000	0.0000 ± 0.0000	0.0000 ± 0.0000
500518	1.400	0.0000 ± 0.0000	0.0000 ± 0.0000	0.0000 ± 0.0000	0.0000 ± 0.0000
500514	1.500	0.0062 ± 0.0022	0.0000 ± 0.0000	0.0000 ± 0.0000	0.0000 ± 0.0000
500545	1.555	0.0055 ± 0.0004	0.0000 ± 0.0000	0.0000 ± 0.0000	0.0000 ± 0.0000
500548	1.560	0.0053 ± 0.0004	0.0000 ± 0.0000	0.0000 ± 0.0000	0.0000 ± 0.0000
500541	1.570	0.0055 ± 0.0005	0.0000 ± 0.0000	0.0000 ± 0.0000	0.0000 ± 0.0000
500540	1.575	0.0045 ± 0.0005	0.0000 ± 0.0000	0.0000 ± 0.0000	0.0000 ± 0.0000
500539	1.580	0.0043 ± 0.0004	0.0000 ± 0.0000	0.0000 ± 0.0000	0.0000 ± 0.0000
500537	1.590	0.0039 ± 0.0004	0.0000 ± 0.0000	0.0000 ± 0.0000	0.0000 ± 0.0000
500533	1.600	0.0038 ± 0.0003	0.0000 ± 0.0000	0.0000 ± 0.0000	0.0000 ± 0.0000
500534	1.605	0.0039 ± 0.0003	0.0000 ± 0.0000	0.0000 ± 0.0000	0.0000 ± 0.0000
500535	1.610	0.0039 ± 0.0003	0.0000 ± 0.0000	0.0000 ± 0.0000	0.0000 ± 0.0000
500536	1.630	0.0038 ± 0.0002	0.0000 ± 0.0000	0.0000 ± 0.0000	0.0000 ± 0.0000
500544	1.650	0.0035 ± 0.0002	0.0000 ± 0.0000	0.0000 ± 0.0000	0.0000 ± 0.0000
500530	1.700	0.0030 ± 0.0002	0.0000 ± 0.0000	0.0000 ± 0.0000	0.0000 ± 0.0000
500231	2.100	0.0030 ± 0.0002	0.0014 ± 0.0002	0.0020 ± 0.0002	0.0000 ± 0.0000
500233	2.300	0.0027 ± 0.0002	0.0004 ± 0.0003	0.0015 ± 0.0001	0.0000 ± 0.0000
500239	2.500	0.0027 ± 0.0001	0.0005 ± 0.0001	0.0011 ± 0.0001	0.0003 ± 0.0001
500235	2.700	0.0020 ± 0.0004	0.0003 ± 0.0001	0.0011 ± 0.0002	0.0000 ± 0.0000
500238	2.900	0.0017 ± 0.0001	0.0003 ± 0.0001	0.0009 ± 0.0001	0.0000 ± 0.0000
500240	3.100	0.0011 ± 0.0001	0.0004 ± 0.0001	0.0006 ± 0.0001	0.0005 ± 0.0001
500241	3.300	0.0010 ± 0.0001	0.0004 ± 0.0001	0.0006 ± 0.0001	0.0000 ± 0.0000
500242	3.500	0.0009 ± 0.0001	0.0004 ± 0.0001	0.0007 ± 0.0001	0.0000 ± 0.0000
500243	3.700	0.0008 ± 0.0001	0.0003 ± 0.0001	0.0006 ± 0.0001	0.0003 ± 0.0001
500244	3.900	0.0007 ± 0.0001	0.0003 ± 0.0001	0.0006 ± 0.0001	0.0003 ± 0.0001
500245	4.100	0.0006 ± 0.0001	0.0003 ± 0.0001	0.0006 ± 0.0001	0.0002 ± 0.0001
500247	4.300	0.0005 ± 0.0001	0.0003 ± 0.0001	0.0005 ± 0.0001	0.0003 ± 0.0001
500249	4.700	0.0004 ± 0.0001	0.0002 ± 0.0001	0.0004 ± 0.0001	0.0002 ± 0.0001
500250	5.100	0.0003 ± 0.0001	0.0001 ± 0.0000	0.0004 ± 0.0001	0.0003 ± 0.0000
500251	5.500	0.0002 ± 0.0000	0.0001 ± 0.0000	0.0005 ± 0.0001	0.0005 ± 0.0001
500252	5.900	0.0002 ± 0.0000	0.0001 ± 0.0000	0.0004 ± 0.0000	0.0004 ± 0.0000

Table 4.2: Fitted escape and fluorescent line parameters for *ssd\_x*.

runid	$E_{MC}$	$E_{fit}$ (keV)	t2norm	t2par	shelfnm
500379	0.400	0.398 ± 0.0000	0.0000 ± 0.0000	1.0020 ± 0.0000	0.0000 ± 0.0000
500354	0.450	0.446 ± 0.0000	0.0000 ± 0.0000	1.0020 ± 0.0000	0.0000 ± 0.0000
500357	0.500	0.498 ± 0.0000	0.0000 ± 0.0000	1.0020 ± 0.0000	0.0000 ± 0.0000
500394	0.548	0.547 ± 0.0000	0.0308 ± 0.0000	1.0020 ± 0.0000	0.0000 ± 0.0000
500358	0.600	0.599 ± 0.0000	0.0254 ± 0.0006	1.0120 ± 0.0031	0.0000 ± 0.0000
500362	0.700	0.699 ± 0.0000	0.0205 ± 0.0056	1.0180 ± 0.0083	0.0000 ± 0.0188
500363	0.800	0.801 ± 0.0000	0.0105 ± 0.0009	1.0270 ± 0.0061	0.0097 ± 0.0014
500396	0.900	0.902 ± 0.0000	0.0153 ± 0.0030	1.0600 ± 0.0070	0.0110 ± 0.0003
500366	1.000	1.002 ± 0.0000	0.0233 ± 0.0034	1.0640 ± 0.0050	0.0091 ± 0.0002
500368	1.100	1.103 ± 0.0000	0.0276 ± 0.0034	1.0630 ± 0.0040	0.0080 ± 0.0002
500401	1.200	1.204 ± 0.0000	0.0335 ± 0.0030	1.0600 ± 0.0026	0.0075 ± 0.0002
500399	1.212	1.216 ± 0.0000	0.0347 ± 0.0031	1.0620 ± 0.0026	0.0074 ± 0.0001
500398	1.234	1.233 ± 0.0000	0.2224 ± 0.0121	1.0880 ± 0.0018	0.0195 ± 0.0003
500397	1.400	1.398 ± 0.0000	0.5291 ± 0.0220	1.0840 ± 0.0010	0.0391 ± 0.0007
500395	1.500	1.497 ± 0.0000	0.4726 ± 0.0169	1.0740 ± 0.0008	0.0397 ± 0.0006
500393	1.555	1.556 ± 0.0000	0.7628 ± 0.0370	1.0870 ± 0.0009	0.0441 ± 0.0011
500391	1.560	1.561 ± 0.0000	0.7812 ± 0.0413	1.0880 ± 0.0010	0.0469 ± 0.0012
500390	1.570	1.574 ± 0.0000	1.0610 ± 0.0679	1.0880 ± 0.0010	0.0838 ± 0.0030
500389	1.575	1.579 ± 0.0000	0.9983 ± 0.0557	1.0850 ± 0.0009	0.0774 ± 0.0023
500388	1.580	1.583 ± 0.0000	0.9487 ± 0.0531	1.0860 ± 0.0009	0.0724 ± 0.0022
500387	1.590	1.592 ± 0.0000	0.8038 ± 0.0415	1.0850 ± 0.0009	0.0590 ± 0.0015
500386	1.600	1.603 ± 0.0000	0.7713 ± 0.0358	1.0810 ± 0.0009	0.0626 ± 0.0015
500385	1.605	1.608 ± 0.0000	0.8068 ± 0.0405	1.0830 ± 0.0009	0.0630 ± 0.0016
500384	1.610	1.613 ± 0.0000	0.7666 ± 0.0375	1.0810 ± 0.0009	0.0610 ± 0.0015
500383	1.630	1.632 ± 0.0000	0.6993 ± 0.0318	1.0790 ± 0.0009	0.0567 ± 0.0013
500382	1.650	1.652 ± 0.0000	0.6415 ± 0.0221	1.0750 ± 0.0007	0.0551 ± 0.0009
500381	1.700	1.700 ± 0.0000	0.4257 ± 0.0118	1.0650 ± 0.0006	0.0462 ± 0.0006
500331	2.100	2.103 ± 0.0000	1.0120 ± 0.0926	1.0780 ± 0.0007	0.0333 ± 0.0017
500330	2.300	2.290 ± 0.0000	0.7967 ± 0.0572	1.0750 ± 0.0007	0.0257 ± 0.0009
500329	2.500	2.478 ± 0.0000	0.5816 ± 0.0334	1.0730 ± 0.0007	0.0199 ± 0.0005
500328	2.700	2.667 ± 0.0000	0.5074 ± 0.0287	1.0710 ± 0.0007	0.0184 ± 0.0005
500327	2.900	2.857 ± 0.0000	0.4370 ± 0.0231	1.0700 ± 0.0008	0.0167 ± 0.0004
500324	3.100	3.047 ± 0.0000	0.3696 ± 0.0176	1.0680 ± 0.0007	0.0146 ± 0.0003
500323	3.300	3.238 ± 0.0000	0.2731 ± 0.0131	1.0650 ± 0.0008	0.0123 ± 0.0002
500322	3.500	3.428 ± 0.0000	0.2867 ± 0.0136	1.0650 ± 0.0008	0.0121 ± 0.0002
500318	4.100	3.998 ± 0.0000	0.1998 ± 0.0086	1.0630 ± 0.0007	0.0092 ± 0.0001
500316	4.300	4.188 ± 0.0000	0.2104 ± 0.0104	1.0650 ± 0.0009	0.0090 ± 0.0002
500315	4.500	4.377 ± 0.0000	0.1725 ± 0.0092	1.0630 ± 0.0010	0.0077 ± 0.0001
500314	4.700	4.566 ± 0.0000	0.1433 ± 0.0071	1.0610 ± 0.0009	0.0074 ± 0.0001
500313	4.900	4.756 ± 0.0000	0.1472 ± 0.0077	1.0610 ± 0.0010	0.0075 ± 0.0001
500311	5.300	5.134 ± 0.0000	0.1346 ± 0.0079	1.0630 ± 0.0011	0.0066 ± 0.0001
500310	5.500	5.322 ± 0.0000	0.1279 ± 0.0076	1.0610 ± 0.0011	0.0062 ± 0.0001
500309	5.700	5.509 ± 0.0000	0.1157 ± 0.0072	1.0600 ± 0.0012	0.0053 ± 0.0001
500308	5.900	5.697 ± 0.0000	0.1013 ± 0.0063	1.0590 ± 0.0012	0.0055 ± 0.0001

Table 4.3: Fitted energy, rising (low-energy) tail and shelf parameters for *ssd\_5*.

runid	$E_{MC}$	L2norm	L3norm	L4norm	L5norm
500379	0.400	0.0000 ± 0.0000	0.0000 ± 0.0000	0.0000 ± 0.0000	0.0000 ± 0.0000
500354	0.450	0.0000 ± 0.0000	0.0000 ± 0.0000	0.0000 ± 0.0000	0.0000 ± 0.0000
500357	0.500	0.0000 ± 0.0000	0.0000 ± 0.0000	0.0000 ± 0.0000	0.0000 ± 0.0000
500394	0.548	0.0000 ± 0.0000	0.0000 ± 0.0000	0.0000 ± 0.0000	0.0000 ± 0.0000
500358	0.600	0.0000 ± 0.0000	0.0000 ± 0.0000	0.0000 ± 0.0000	0.0000 ± 0.0000
500362	0.700	0.0000 ± 0.0000	0.0000 ± 0.0000	0.0000 ± 0.0000	0.0000 ± 0.0000
500363	0.800	0.0000 ± 0.0000	0.0000 ± 0.0000	0.0000 ± 0.0000	0.0000 ± 0.0000
500396	0.900	0.0000 ± 0.0000	0.0000 ± 0.0000	0.0000 ± 0.0000	0.0000 ± 0.0000
500366	1.000	0.0000 ± 0.0000	0.0000 ± 0.0000	0.0000 ± 0.0000	0.0000 ± 0.0000
500368	1.100	0.0000 ± 0.0000	0.0000 ± 0.0000	0.0000 ± 0.0000	0.0000 ± 0.0000
500401	1.200	0.0000 ± 0.0000	0.0000 ± 0.0000	0.0000 ± 0.0000	0.0000 ± 0.0000
500399	1.212	0.0000 ± 0.0000	0.0000 ± 0.0000	0.0000 ± 0.0000	0.0000 ± 0.0000
500398	1.234	0.0000 ± 0.0000	0.0000 ± 0.0000	0.0000 ± 0.0000	0.0000 ± 0.0000
500397	1.400	0.0000 ± 0.0000	0.0000 ± 0.0000	0.0000 ± 0.0000	0.0000 ± 0.0000
500395	1.500	0.0039 ± 0.0007	0.0000 ± 0.0000	0.0000 ± 0.0000	0.0000 ± 0.0000
500393	1.555	0.0033 ± 0.0003	0.0000 ± 0.0000	0.0000 ± 0.0000	0.0000 ± 0.0000
500391	1.560	0.0033 ± 0.0003	0.0000 ± 0.0000	0.0000 ± 0.0000	0.0000 ± 0.0000
500390	1.570	0.0032 ± 0.0003	0.0000 ± 0.0000	0.0000 ± 0.0000	0.0000 ± 0.0000
500389	1.575	0.0032 ± 0.0003	0.0000 ± 0.0000	0.0000 ± 0.0000	0.0000 ± 0.0000
500388	1.580	0.0033 ± 0.0003	0.0000 ± 0.0000	0.0000 ± 0.0000	0.0000 ± 0.0000
500387	1.590	0.0029 ± 0.0002	0.0000 ± 0.0000	0.0000 ± 0.0000	0.0000 ± 0.0000
500386	1.600	0.0030 ± 0.0002	0.0000 ± 0.0000	0.0000 ± 0.0000	0.0000 ± 0.0000
500385	1.605	0.0029 ± 0.0002	0.0000 ± 0.0000	0.0000 ± 0.0000	0.0000 ± 0.0000
500384	1.610	0.0027 ± 0.0002	0.0000 ± 0.0000	0.0000 ± 0.0000	0.0000 ± 0.0000
500383	1.630	0.0026 ± 0.0002	0.0000 ± 0.0000	0.0000 ± 0.0000	0.0000 ± 0.0000
500382	1.650	0.0028 ± 0.0002	0.0000 ± 0.0000	0.0000 ± 0.0000	0.0000 ± 0.0000
500381	1.700	0.0023 ± 0.0002	0.0000 ± 0.0000	0.0000 ± 0.0000	0.0000 ± 0.0000
500331	2.100	0.0028 ± 0.0001	0.0011 ± 0.0001	0.0022 ± 0.0001	0.0000 ± 0.0000
500330	2.300	0.0020 ± 0.0002	0.0009 ± 0.0001	0.0018 ± 0.0001	0.0002 ± 0.0001
500329	2.500	0.0024 ± 0.0001	0.0002 ± 0.0001	0.0016 ± 0.0001	0.0004 ± 0.0001
500328	2.700	0.0017 ± 0.0001	0.0001 ± 0.0001	0.0012 ± 0.0000	0.0004 ± 0.0001
500327	2.900	0.0015 ± 0.0001	0.0002 ± 0.0001	0.0009 ± 0.0001	0.0003 ± 0.0001
500324	3.100	0.0014 ± 0.0001	0.0002 ± 0.0001	0.0008 ± 0.0001	0.0002 ± 0.0001
500323	3.300	0.0011 ± 0.0001	0.0002 ± 0.0001	0.0006 ± 0.0001	0.0000 ± 0.0000
500322	3.500	0.0011 ± 0.0001	0.0002 ± 0.0001	0.0006 ± 0.0001	0.0000 ± 0.0000
500318	4.100	0.0007 ± 0.0001	0.0002 ± 0.0000	0.0005 ± 0.0001	0.0002 ± 0.0000
500316	4.300	0.0006 ± 0.0001	0.0002 ± 0.0000	0.0005 ± 0.0001	0.0002 ± 0.0000
500315	4.500	0.0006 ± 0.0001	0.0001 ± 0.0000	0.0004 ± 0.0001	0.0002 ± 0.0000
500314	4.700	0.0005 ± 0.0001	0.0001 ± 0.0000	0.0004 ± 0.0000	0.0002 ± 0.0000
500313	4.900	0.0004 ± 0.0001	0.0001 ± 0.0000	0.0003 ± 0.0000	0.0002 ± 0.0000
500311	5.300	0.0003 ± 0.0000	0.0001 ± 0.0000	0.0003 ± 0.0000	0.0001 ± 0.0000
500310	5.500	0.0004 ± 0.0000	0.0001 ± 0.0000	0.0002 ± 0.0000	0.0002 ± 0.0000
500309	5.700	0.0003 ± 0.0000	0.0000 ± 0.0000	0.0002 ± 0.0000	0.0001 ± 0.0000
500308	5.900	0.0003 ± 0.0000	0.0000 ± 0.0000	0.0002 ± 0.0000	0.0001 ± 0.0000

Table 4.4: Fitted escape and fluorescent line parameters for *ssd\_5*.

phase	detector	fano	broad (chan)
sx700	ssd_5	0.1140	11.87
sx700	ssd_x	0.1450	14.20
kmc	ssd_5	0.1140	10.92
kmc	ssd_x	0.1450	13.23

Table 4.5: Detector resolution parameters: Fano factor and electronic broadening.

resolution than *ssd\_x*, i.e., a narrower electronic broadening and smaller Fano factor. The higher values of electronic broadening for *ssd\_x* are most likely due to a higher leakage current on the crystal surface for this detector, as it was subjected to possible surface contamination while undergoing several repairs. The Fano factor of 0.114 for *ssd\_5* is consistent with values reported by Knoll (1989) for germanium. The Fano factor for *ssd\_x*, 0.145, is a little larger than expected. This is surprising considering the two crystals were presumably cut from the same boule and should have similar bulk properties. However, the result is undeniable: *ssd\_x* has poorer energy resolution than *ssd\_5*.

Determination of the Fano and the electronic broadening values was one of the most challenging part of the fitting procedure. We initially fit the spectra recorded at the KMC beamline for x-ray energies higher than 3 keV, where the peak pileup located at twice the main-peak pulse-height is a purely pileup peak, free of higher order photon peaks from the monochromator. The width of these pileup peaks is a sum in quadrature of two Fano broadening,  $\sigma_f$ , terms and one electronic broadening,  $\sigma_e$ , term. Whereas, the width of the main line peak is the quadratic sum of only one Fano broadening term and one electronic broadening term. This difference in width made it possible to get good starting values for the Fano factor and the electronic broadening. Then, using these starting values and keeping the Fano factor fixed, all the KMC spectra (in the energy range 2.1-5.9 keV) for each detector were fitted while the electronic broadening parameter was allowed to float. Once the series of spectra were fitted, the trend of the electronic broadening parameter could be plotted as a function of energy. If the Fano factor and the electronic broadening were correct, there would be no energy dependence on the broad parameter. If there were an energy dependence on the broad parameter, then a subsequent change in the Fano factor could be estimated. After several iterations, the Fano factor could be determined. The value of the Fano factor determined by this procedure was then used as a known value for fitting the spectra recorded at the SX700 beamline (in the energy range 0.4-1.7 keV). The electronic broadening values listed in Table 4.5 are the average values for each set of measurements, calculated from the energy-independent values (from the final iteration that showed no energy dependence trend for the electronic broadening).

The energy scale for the *ssd\_5* detector was obtained from a built-in radioactive source, consisting of an Fe target excited by a  $^{244}\text{Cm}$   $\alpha$ -emitter, which was located on the aperture wheel. The pulse height spectra of radiation from this source were recorded at different times during the course of data recording at the KMC, X700, and 12-20 beamlines for energy calibration as well as for monitoring the possible build-up of ice on the detector surface (as the detector crystal is cooled down to liquid nitrogen temperature, it acts as a cold trap). Figure 4.4 shows the pulse-height spectrum of the radiation from this built-in source. The peak positions of the following lines were fitted to determine the energy scale parameters: Fe  $L\alpha$  and  $L\beta$  lines (at 0.7050 and 0.7185 keV), Al  $K\alpha$  lines (1.4866 keV), Ge escape lines at 4.392 and 4.423 keV, Cr  $K\alpha$  lines (at 5.4055 and 5.4147 keV), Fe  $K\alpha$  lines (at 6.3908 and 6.4038 keV), Fe  $K\beta$  lines (at 7.05798 keV), Ge escape lines at 8.407 and 8.438 keV, Pu  $L\alpha$  lines (at 14.2786 and 14.0842 keV), and Pu  $L\beta_2$  line (at 17.2553 keV). The following intensity-ratio constraints were used to facilitate the fitting:  $FeL\beta/FeL\alpha = 0.225$ ,

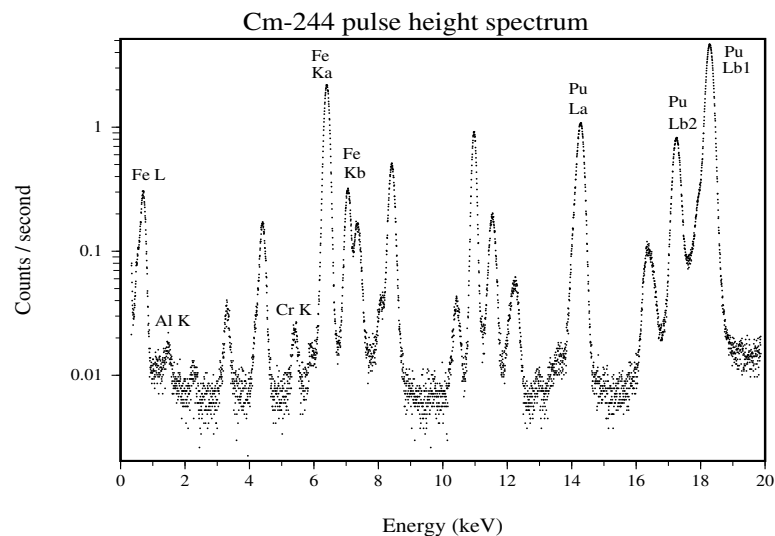


Figure 4.4: The pulse-height spectrum of radiation from an Fe target excited by a  $^{244}\text{Cm}$   $\alpha$ -emitter.

$\text{CrK}\alpha_2/\text{CrK}\alpha_1 = 0.500$ ,  $\text{FeK}\alpha_2/\text{FeK}\alpha_1 = 0.500$ , and  $\text{PuL}\alpha_2/\text{PuL}\alpha_1 = 0.100$ . These ratios include the effects of 2 micron of ice, 2 micron of Parylene, and 0.3 micron of aluminum filters.

Determination of the energy scale parameters for the `ssd_x` proved to be more challenging since there was no built-in radioactive source in this detector. The energy scale for the spectra recorded at the KMC beamline were determined from the known spectral features such as Ge escape and fluorescence, Al fluorescence, and the peak pileup. Since the peak pileup is at twice the pulse height (but not necessarily twice the channel number) of the main line, it was possible to determine the channel offset (zero point of the energy scale) from the channel locations of the main peak and the pileup peak. The peak locations of the escape and fluorescent lines helped in determining the gain parameter of the scale. For the spectra recorded at the SX700 beamline, the spectral features mentioned above could not be used to determine the energy scale. In this case, those features were either much weaker or overlapping with other features in the spectra. However, since the energy scale of the SX700 grating monochromator was calibrated by PTB to within  $\pm 2$  eV, we used the energy settings of this monochromator as the energy standards in our fits.

The fitted energy scale parameters, gain and channel offset (choff) for both detectors are summarized in Table 4.6. The channel offset values in this table are the average values of the fitted values for each set of measurement. The channel offset is nearly constant for each set. The energy scales for the `ssd_5` are valid for the entire energy range of the white light spectra. The estimated energy uncertainty for this energy range (i.e. 0.4-10 keV) is  $\pm 5$  eV. This uncertainty is mostly due to the uncertainty in the energy offset which is more influenced by the low-energy peaks in the  $^{244}\text{Cm}$  spectra. The uncertainty in the energy gain is much smaller. For the `ssd_x` detector, however, the given energy scales have an uncertainty of  $\pm 8$  eV for the energy range 0.4-1.7 keV.

phase	dates	detector	gain (chan/pair)	choff (chan)
D	961230–970126	ssd_5	0.5914	–12.02
D	961230–970126	ssd_x	0.6039	–12.92
E	970128–970211	ssd_5	0.5905	–10.31
E	970128–970211	ssd_x	0.6119	–12.78
J	970618–970626	ssd_5	0.5965	–10.84
J	970618–970626	ssd_x	0.6211	–12.84
kmc	971013–971017	ssd_5	0.6052	–8.19
kmc	971013–971017	ssd_x	0.6100	–27.85
sx700	971020–971026	ssd_5	0.6048	–7.09
sx700	971020–971026	ssd_x	0.6161	–26.13
12-20	971020–971026	ssd_5	0.6050	–6.65

Table 4.6: Energy scale parameters for each phase of SSD use.

The uncertainty for higher energies are much higher and increases with energy. This is due to the fact that for this detector, as stated above, there were no energy calibration standards for energies higher than 1.7 keV, and it was, further, not possible to get a unique set of values for the gain and channel offset parameters in the 0.4-1.7 KeV range, where the energy settings of the SX700 grating monochromator were used as calibration standards. The difference between monochromator energy settings and the corresponding fitted energy values for the main line for both detectors are shown in Figure 4.5. The upper panel is for the measurements with the SX700 grating monochromator, and the lower panel is for measurements with the KMC Si double crystal monochromator, which has much less accurate energy scale than the grating monochromator.

Plots of the response function parameters for the low-energy tail and shelf as well as the escape and fluorescent lines as a function of energy for both detectors are shown in Figures 4.6–4.8. The upper panel in Figure 4.6 shows the tail norm (counts in the tail) relative to the total number of counts in the main peak, and the lower panel shows the tail slope parameter. As can be seen in this figure, for energies higher than 2 keV, the `ssd_5` detector has a slightly larger, but faster decaying (sharper), tail contribution than `ssd_x`. The energy dependence of the tails for both detectors in this energy range agree qualitatively with the energy dependence of Ge atomic photo-absorption cross section. However, at lower energies the the energy dependence of the tail for `ssd_5` is drastically different from that of `ssd_x`. Both tails drop sharply at the Ge-L edge. Below the Ge edge, the `ssd_x` tail rises in agreement with the Ge absorption cross section, but the `ssd_5` tail decreases to even lower values. Both tails have structures at the Al-K edge, showing the contribution of the Al layers on the detector crystal and the radiation shield. There is a sharp drop in the tail norm for `ssd_5` in the energy range 1.75-1.85 KeV, located in the energy region separating the KMC measurements (with the Si crystal) from the SX700 measurements. This feature is not present in the `ssd_x` tail. Since both detectors have identical filters and contact material, we first suspected this feature to be due to a change in the detector electronics, when switching from the KMC beamline to the SX700 beamline. However, by inspecting the width of the pulser peak in all the spectra recorded at both beamlines, we have ruled out such a possibility. Further, the analysis of another set of measurements, in the energy range 1.7-5.1 keV, which were taken prior to the measurements with the Si monochromator, produced the same tail behavior. The four data points in the energy range 1.7-2.1 keV for the `ssd_5` detector in Figure 4.6 are from the data taken by the InSb monochromator.

The low-energy tails for both detectors have some small tail-pileup contributions. This was

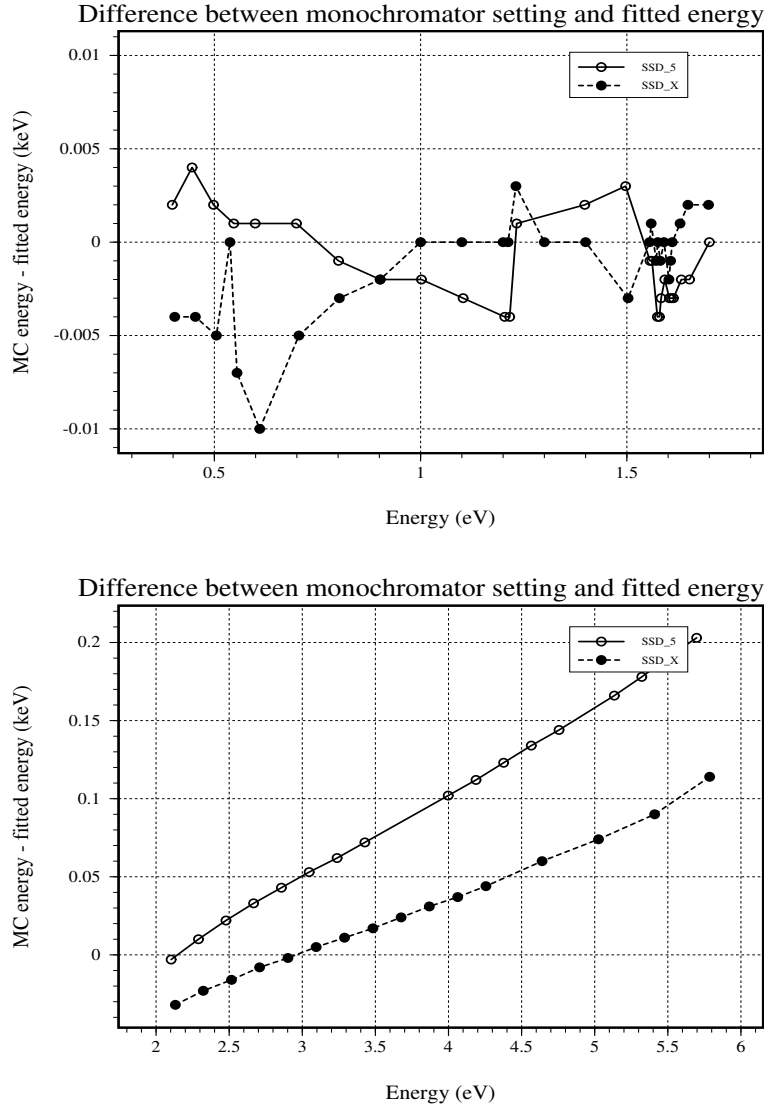


Figure 4.5: The difference between the monochromator energy setting and the fitted energy.

discovered by checking the pulser peak in the spectra. The pulser peak in all the spectra, except for `ssd_5` spectra taken at SX700, show some low-energy tailing. This kind of tailing in the pulser peak is an indication of the presence of tail pileup.

Figure 4.7 shows the shelf norm (counts in the shelf) relative to the total number of counts in the main peak for both detectors. As is seen in this figure, for energies above 0.8 keV, both detectors have the same general trend for the energy dependence of the shelf. This trend is in agreement with the model calculation of Kraft et al. (1997), which is based on the calculation of energy losses for the transmission of photo- and Auger electrons through the detector dead layer and contact material. For energies below 0.8 keV, the shelf for the `ssd_5` detector decreases, while the shelf for `ssd_x` increases in agreement with the calculation of Kraft et al. (1997). The disagreement between the two detectors at lower energies in this case, as well as in the case for the low-energy tail, as discussed above, might be related to the fact that at these low energies the detector noise partially masks the tail and shelf features in this part of the pulse-height spectra, and consequently the response-function model does not fit the data well. This can be seen in Figure 4.9, where the chi-squared of the fits for spectra at lower energies have very high values, specially those for the `ssd_5` detector.

The secondary features of the response function: Ge-L escape, Al-K and Ge-L fluorescent lines, are shown in Figure 4.8, where the norm for each line, relative to the total number of counts in the corresponding spectrum, has been plotted as a function of energy. The Si-K fluorescent line shown in this figure is not part of the detector response function, since it originated from the Si double crystal monochromator, not the detector. As can be seen in the figure, these lines are very weak, and the most dominant line, Ge-L escape, has values less than 0.6% of the total counts recorded by the detector.

In Chapter 11, SSD carbon continuum spectra from various phases of XRCF testing for both SSD are described. By fitting the energy scale to the known energies and observed pulse heights of impurity lines, energy scale constants can be derived. The parameters are given in Table 4.6. The fitting formula used there is:

$$\text{Energy} = a + b \times \text{channel}. \quad (4.7)$$

In the JMKmod software, the relationship between energy and channel is:

$$\text{channel} = \text{Energy} \times \text{gain}/i_{\text{pot}} + \text{ch\_off} + \text{gain} + 1, \quad (4.8)$$

where  $i_{\text{pot}}$  is the ionization energy (0.003 keV per ion pair). It follows that

$$\text{gain} = i_{\text{pot}}/b, \quad (4.9)$$

and

$$\text{ch\_off} = -(b + 1) - (i_{\text{pot}}/b) \times a. \quad (4.10)$$

We have taken the fitting results presented above, and produced an XSPEC-compatible response matrix for each of the two SSD detectors. Since the energy scale of each detector is different in each phase of the testing (because of slightly different noise environments or amplifier settings), a separate matrix is required for use with the data from each phase of the testing. Because of limits on the number of non-zero response matrix elements, we elected to create  $1024 \times 1024$  matrices, which necessitates the binning of the raw data into 4-channel bins. The input parameters were linearly interpolated between those presented above.

A response matrix  $R_{ij}$  is a set of response functions, one for each of a number of energy bins  $E_j$ . Given that a photon of energy  $E_j$  is detected, the element  $R_{ij}$  is the probability that the



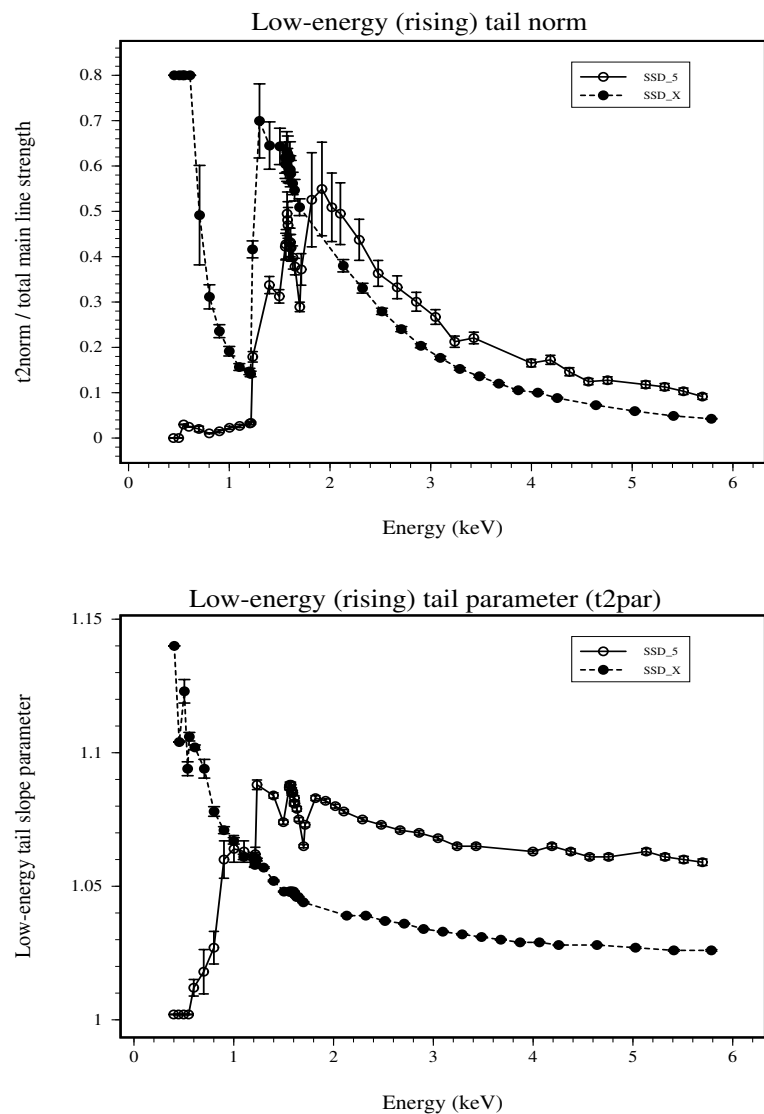


Figure 4.6: Fitted low-energy (rising) tail parameters for `ssd_5` and `ssd_x`. The upper panel shows the tail norm (counts in the tail), plotted as a fraction of the total number of counts in the main peak. The lower panel shows the corresponding values of the slope parameter.

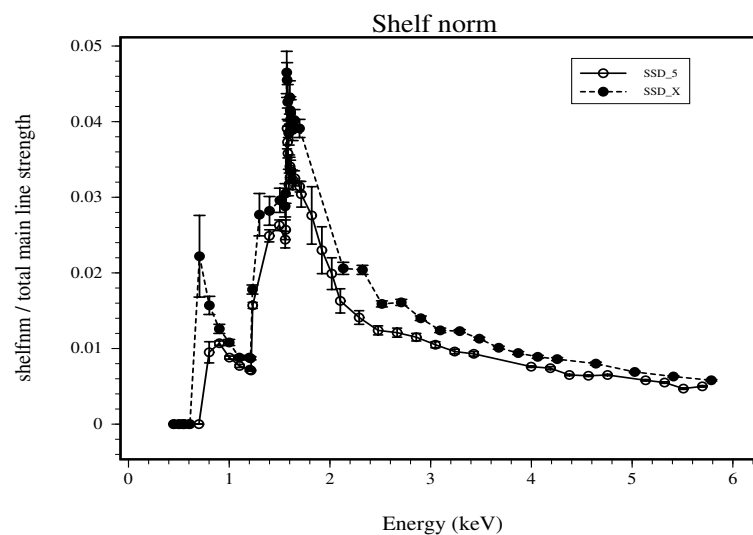


Figure 4.7: Fitted shelf norm (counts in the shelf) for `ssd_5` and `ssd_x`, plotted as a fraction of the total number of counts in the main peak.

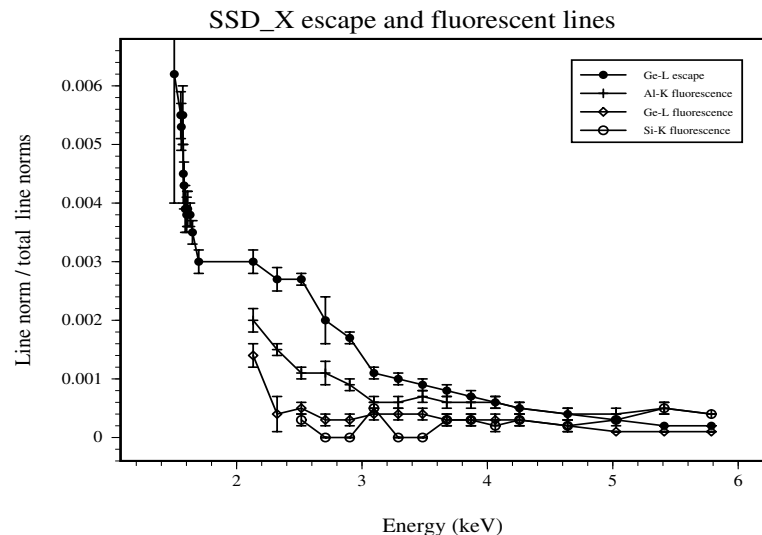
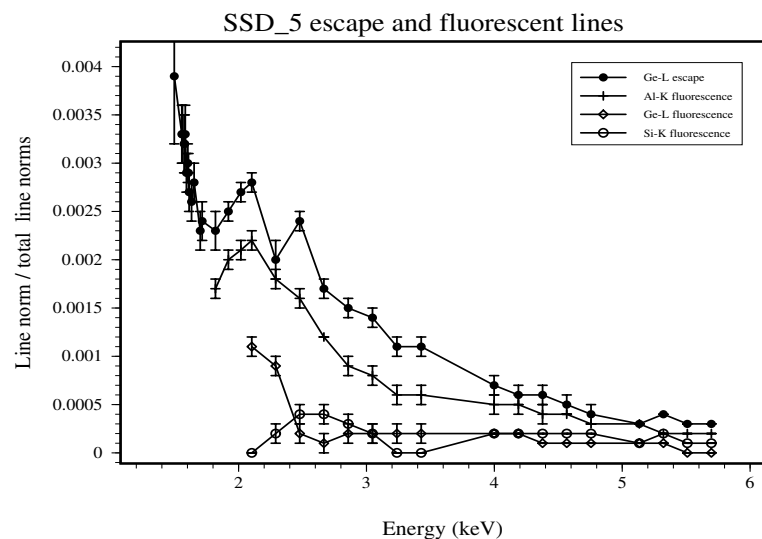


Figure 4.8: Fitted escape and fluorescent line norms for *ssd5* (upper panel) and *ssd\_x* (lower panel), plotted as a fraction of the total number of counts.

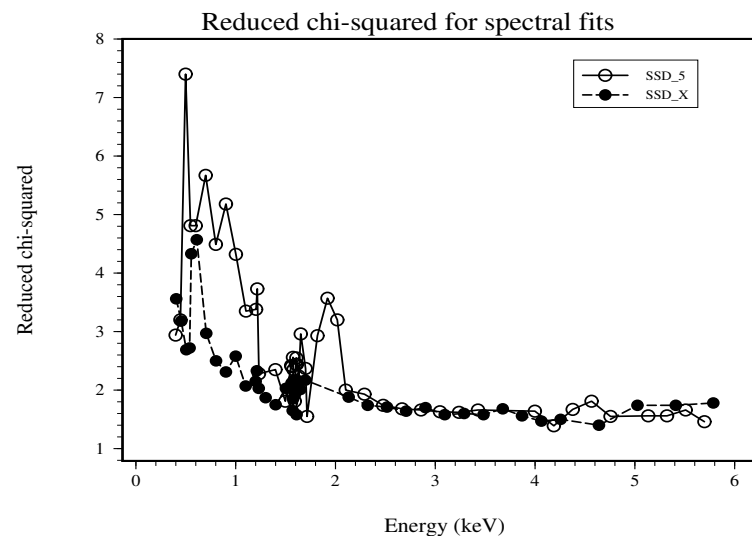


Figure 4.9: Reduced chi-squared  $\chi^2$  values for the fitted regions of the spectra.

detector emits a pulse of pulse height  $E_i$ . Thus each column of the matrix is just the (normalized) detector response function for monoenergetic photons of a given energy. Energy dependent quantum efficiency effects are accounted for in a separate computer file, known as an Ancillary Response Function (ARF). See the next section for the derivation of the SSD quantum efficiency.

## 4.5 Detector Efficiency vs. Energy Narrow Band

The detector efficiency as a function of energy over the range from 400 eV to 1.7 keV was measured on the SX700 Grating monochromator beam line. These data also provided a measure of the response function of the detector from 400 eV to 1.7 keV which include some energies that were not reachable by the KMC beam line. The flux recorded by the detector on this beam line can be compared to the transfer standard calibrated photodiode (traceable to the cryogenic electrical substitution radiometer) in the beam line to measure the detector efficiency over this energy range.

In the calibration, we scanned the monochromator from 400 eV to 1.7 keV with carefully selected steps taken around the O-K, Ge-L and Al-K absorption edges to capture fine structure such as EXAFS. The oxygen is from the ice, the Ge is from any possible dead layer on the front of the detector face, and the aluminum is from the IR shield and the Aluminum contact on the detector surface. We fitted the main peak, including the rising tail and shelf to determine the counts in this part of the spectrum. The counts under the germanium escape peak as well as the counts under the aluminum and germanium fluorescent peaks were added to the main-peak counts. Then these counts were corrected for pileup effects. The interpeak, peak, and pulser pileup events were determined by inspecting each individual spectrum, setting regions of interest containing these

events, and summing the counts in the corresponding regions of interest. Special care was taken to exclude counts due to the monochromator higher order lines. The interpeak and peak pileup counts are actually two events registered as one and thus were multiplied by two. However, the pulser-pileup events were not counted twice since each of these events involves one pulse from the pulser and one pulse from the detector. since the count rate for all of the recorded spectra were around 1000 counts/second, the effect of higher order pileups involving more than two pulses was negligible and was not considered.

$$\begin{aligned} \text{Total Recorded Counts} = & \text{Main Peak} + \text{Escape Peak} + \text{Fluorescent Peaks} + \\ & 2(\text{Interpeak} + \text{Peak Pileup}) + \text{Pulser Pileup} \end{aligned} \quad (4.11)$$

Next the total counts were corrected for dead time by summing the counts in the pulser and pulser-pileup peaks and dividing by the number of injected pulser pulses. This gives the live time which is divided into the total recorded counts. The result is the measured flux incident on the detector crystal. This value was compared with the flux as measured by the PTB photodiode to determine the detector efficiency for the given energies.

The QE results from the SX700 are shown in Figure 4.10, and the numbers for the measured and fitted quantum efficiencies are in Tables 4.7 and 4.8.

We fitted the QE data for both detectors to a model consisting of the x-ray transmission of the detector windows, which included parylene-N ( $\text{C}_8\text{H}_8$ ) coated with aluminum and ice which builds up on the detector. The Gullikson 1995 version of the optical data (update of Henke et al. (1993)) were used in the model, which was upgraded with data from Tikkanen (1997) to include the extended x-ray absorption fine structures (EXAFS) above the oxygen and aluminum K edges.

The resulting fitted curves are shown in Figure 4.10. The corresponding fitted thicknesses for the window materials are summarized in Table 4.9. These thicknesses were obtained assuming a density of  $2.70 \text{ g cm}^{-3}$  for aluminum, a density of  $1.10 \text{ g cm}^{-3}$  for parylene, and  $0.917 \text{ g cm}^{-3}$  for ice.

The fitted parylene thickness value for *ssd\_5*,  $1.41 \mu\text{m}$ , is close to the expected nominal value of  $1.2 \mu\text{m}$  ( $1 \mu\text{m}$  vacuum barrier window plus a  $0.2 \mu\text{m}$  IR shield). However, the value for *ssd\_x*,  $2.07 \mu\text{m}$ , is much thicker than this nominal value. The fitted aluminum values for both detectors are almost identical but are thicker than the nominal value of  $0.2 \mu\text{m}$  that is expected from the aluminum contact on the detector and the IR shield. The fitted ice value is  $1.58 \mu\text{m}$  for the *ssd\_5* and  $2.37 \mu\text{m}$  for *ssd\_x*. The value for *ssd\_x* is comparable to the  $3 \mu\text{m}$  value found at XRCF from the  $^{244}\text{Cm}$  source data (§11.9). For the *ssd\_5*, a somewhat thinner layer of ice than for *ssd\_x* is reasonable, because we know that it was dehydrated better during its manufacture, and it may have been de-iced more recently before the BESSY measurements.

It is interesting to note that we have not included the possible Ge dead layer as a window material in our fits. Inclusion of such a layer ( $180 \text{ \AA}$  for *ssd\_5* and  $65 \text{ \AA}$  for *ssd\_x*) improves the fits in the region just below the aluminum edge, where the model does not fit the data well. However, the lack of any structure in the data around the Ge-L edge for both detectors clearly does not justify the inclusion of a Ge dead layer. (The edge structure due to the above Ge thicknesses is as much as five times larger than the error in the data.)

The ice thickness on the *ssd\_x* seems to be essentially time-independent during the SX-700 QE measurement run. We know this because of the following exercise: We presumed that the discrepancy between the measured QE and the best-fit parylene/aluminum (ice-free) window transmission was entirely due to ice. This assumption allows one to compute a thickness of ice as a function of runid (and hence energy and time). We find that, at least in the energy range between the oxygen

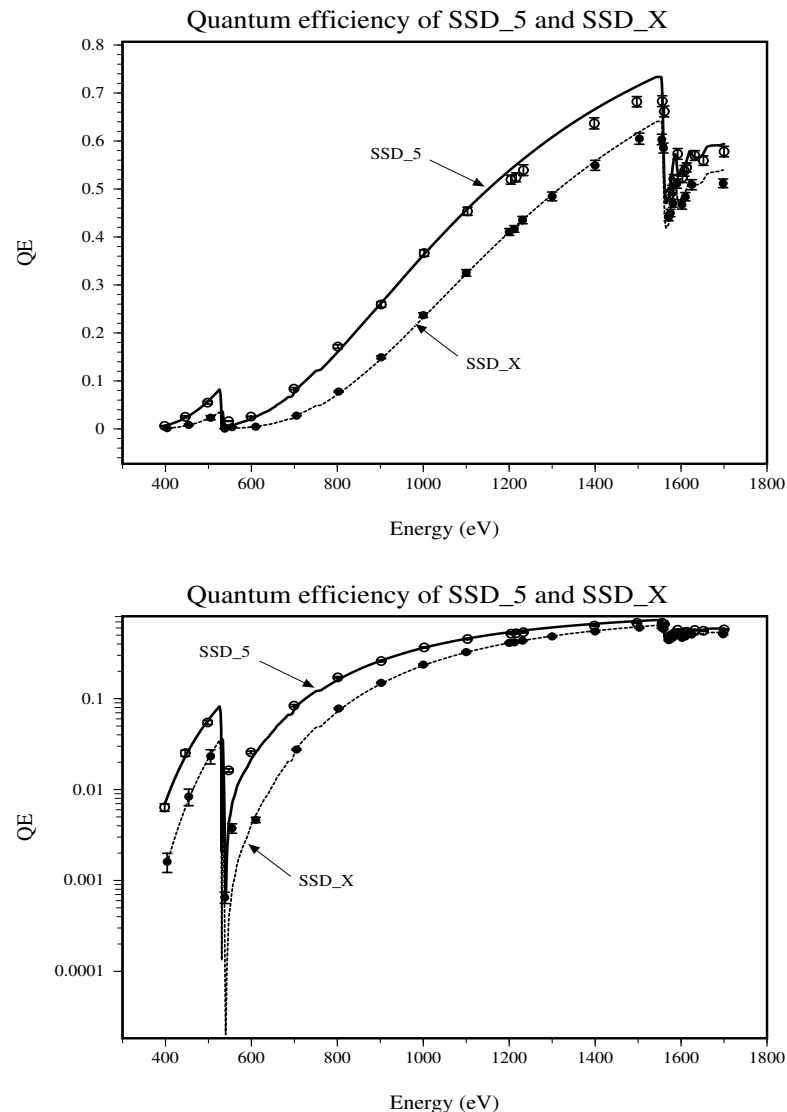


Figure 4.10: Measured QE data from SX700 data and their corresponding fitted curves for *ssd\_5* and *ssd\_x*. The upper panel emphasizes the Al-K edge fine structure, and the lower panel provides a detailed view of the QE near the O-K edge.

Energy (keV)	QE	fit
0.398	0.00636 ± 0.00060	0.00690
0.446	0.02518 ± 0.00195	0.02300
0.498	0.05473 ± 0.00277	0.05692
0.547	0.01627 ± 0.00065	0.00400
0.599	0.02570 ± 0.00081	0.02096
0.699	0.08384 ± 0.00228	0.07412
0.801	0.17159 ± 0.00371	0.15924
0.902	0.25936 ± 0.00563	0.26074
1.002	0.36650 ± 0.00680	0.36229
1.103	0.45353 ± 0.00858	0.45699
1.204	0.51946 ± 0.00948	0.53953
1.216	0.52419 ± 0.00934	0.54851
1.233	0.53920 ± 0.01123	0.56090
1.398	0.63670 ± 0.01157	0.66417
1.497	0.68184 ± 0.01070	0.71269
1.556	0.68295 ± 0.01124	0.70708
1.561	0.66156 ± 0.01123	0.51650
1.574	0.48880 ± 0.00931	0.49843
1.579	0.49781 ± 0.00991	0.53437
1.583	0.52049 ± 0.00943	0.56143
1.592	0.57303 ± 0.01116	0.53505
1.603	0.52386 ± 0.01041	0.54102
1.608	0.53781 ± 0.01110	0.54792
1.613	0.54493 ± 0.00944	0.55920
1.632	0.56975 ± 0.01012	0.56579
1.652	0.55915 ± 0.00982	0.57405
1.700	0.57799 ± 0.01090	0.59389

Table 4.7: Measured and fitted QE values for `ssd_5` from SX700 data.

Energy (keV)	QE	fit
0.404	0.00161 ± 0.00038	0.00155
0.454	0.00837 ± 0.00173	0.00778
0.505	0.02328 ± 0.00415	0.02417
0.538	0.00065 ± 0.00009	0.00021
0.555	0.00376 ± 0.00044	0.00077
0.610	0.00464 ± 0.00031	0.00525
0.705	0.02761 ± 0.00054	0.02866
0.803	0.07788 ± 0.00153	0.07348
0.902	0.14929 ± 0.00290	0.14606
1.000	0.23707 ± 0.00473	0.23195
1.100	0.32521 ± 0.00666	0.32318
1.200	0.41038 ± 0.00708	0.40993
1.212	0.41669 ± 0.00687	0.41992
1.231	0.43522 ± 0.00759	0.43528
1.300	0.48453 ± 0.00911	0.48857
1.400	0.54923 ± 0.01037	0.55785
1.503	0.60485 ± 0.01162	0.61898
1.555	0.60316 ± 0.01098	0.63593
1.559	0.58525 ± 0.01034	0.52220
1.571	0.44097 ± 0.00733	0.42642
1.575	0.44998 ± 0.00764	0.44986
1.581	0.47009 ± 0.00811	0.48823
1.590	0.51108 ± 0.00949	0.49078
1.602	0.46755 ± 0.00950	0.48286
1.610	0.48388 ± 0.00867	0.49335
1.625	0.50890 ± 0.01045	0.51415
1.698	0.51172 ± 0.00902	0.53989

Table 4.8: Measured and fitted QE values for `ssd_x` from SX700 data.

Detector	Al ( $\mu\text{m}$ )	Parylene ( $\mu\text{m}$ )	Ice ( $\mu\text{m}$ )
ssd_5	$0.34 \pm 0.01$	$1.41 \pm 0.02$	$1.58 \pm 0.05$
ssd_x	$0.33 \pm 0.01$	$2.07 \pm 0.04$	$2.37 \pm 0.06$

Table 4.9: Thickness of fitted window material for ssd\_5 and ssd\_x.

and aluminum K edge regions where the Henke tables are a good representation of reality, the ice thickness is independent of runid (and hence of energy and time).

As expected, the fitted QE curves for both detectors approach a value of one at higher energies, where the window material becomes transparent to the higher energy photons. This has been shown in Figure 4.11, where the upper plot shows the QE for ssd\_5 reaching a value of one around 10 keV. The lower plot shows the ratio of ssd5 QE to the QE of ssd\_x. This plot clearly shows that, although the QE of ssdx is lower than the QE for ssd5 at energies lower than 9 keV, both QEs approach the expected value of one near 10 keV.

## 4.6 Q. E. Broad Band: White light Calibration

The broad band QE of the detectors was measured at the PTB 12.20 beam line. This beam line does not contain any optical components and “sees” the raw undispersed synchrotron radiation.

### 4.6.1 The algorithm for calculating the synchrotron radiation spectrum

For the white beam, the calibration is done by calculating the intensity of the synchrotron x-ray emission from first principles, and comparing with the observed counting rate in the detector. We are in the process of doing these comparisons. One important step is the calculation of the beam intensity. The following is a derivation of the predicted flux, given the known operating parameters of the storage ring. We begin with the treatment by J. D. Jackson Jackson (1962) for the power radiated by a single electron.

Using Mathcad, we express the photon spectrum of x-rays emerging from the storage ring tangent point as a function of the ring parameters - electron energy, circulating storage ring current, magnetic field, distance from tangent point to detector, diameter of the circular detector aperture, and the angular displacement of the detector from the orbit plane. We discuss evaluation of the required Bessel functions. In order to calculate the spectrum, we derive expressions for the electron gyroradius, and perform the 2D integration of the flux distribution over the circular detector aperture. We calculate the flux at a set of energies, and we do an integration over all x-ray energies from the detector LLD at 308 eV to a high enough energy to include essentially all the flux.

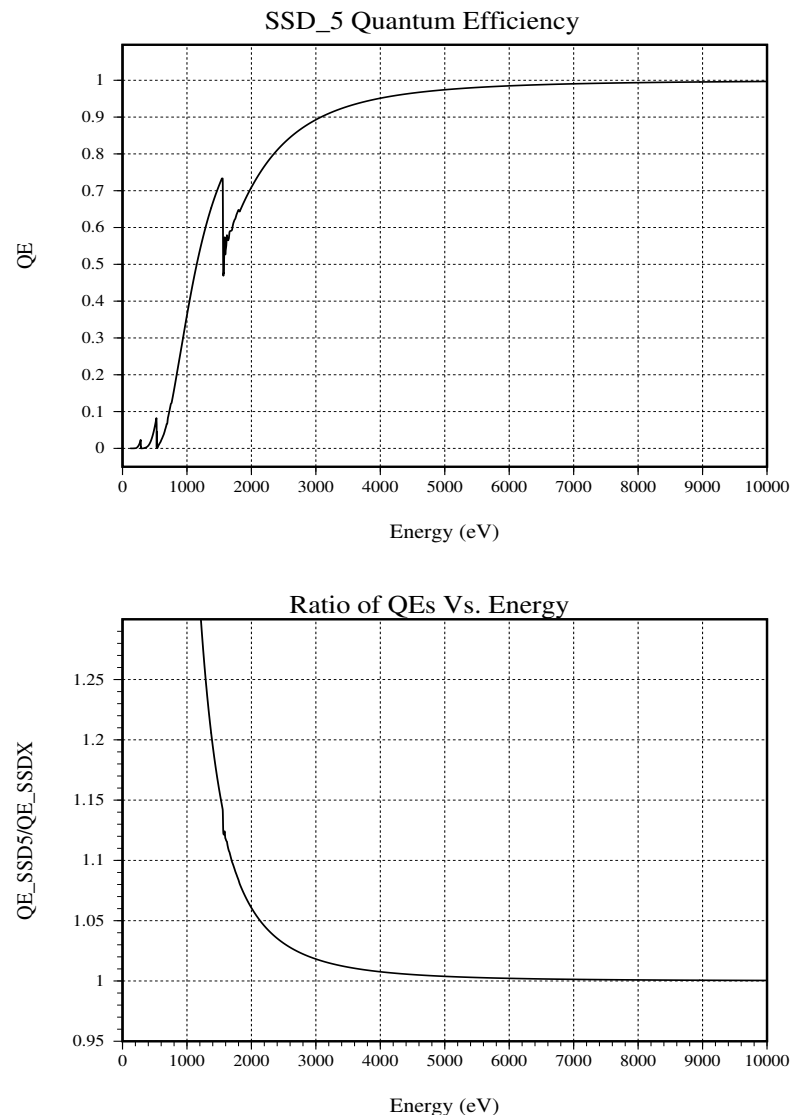


Figure 4.11: The fitted QE curves extended to 10 keV. The upper plot shows the QE curve for ssd5 approaching a value of one at higher energies. The lower plot shows the ratio of QEs as a function of energy.

In section 14, Jackson, uses  $K_n(x)$ , the modified Bessel function of the second kind. We call that BesseK(x,n) following Kostrun's series expansion ( Vaclav O. Kostrun, 1980 N..I.M. 172 371, SCHWINGER program from Thornagel at PTB; also SAOLIB, fn. called kbess.f, maintained by Leon Van Speybroeck, or in mathematica, BesselK[n,x]. PTB's algorithm (Thornagel,private communication) is used here:

Epsilon:= $1 \cdot 10^{-6}$  Step := .0625

```
BesseK(x,v) := 0. if x>88.
                otherwise
                Summand←  $\frac{\exp(-x)}{2}$ 
                Help← Summand
                h← Step
                while [  $\left(\frac{\text{Help}}{\text{Summand}}\right) > \text{Epsilon}$  ]
                | Help←  $\exp(-x \cdot \cosh(h)) \cdot \cosh(v \cdot h)$ 
                | Summand← Summand + Help
                | h← h + Step
                Summand·Step
```

$$K_{13}(x) := \text{BesseK}\left(x, \frac{1}{3}\right) \quad K_{23}(x) := \text{BesseK}\left(x, \frac{2}{3}\right)$$

If we used Mathematica, we could use their built-in routines for  $K_n$  directly. Below, we show that the differences between the two evaluations are  $< 10^{-6}$ .

$K_{23}(.1) = 4.7529605281$  Mathematica gives 4.75296268

$$\text{del} := \frac{K_{23}(.1) - 4.75296268}{4.75296268} \quad \text{del} = -4.5275294 \cdot 10^{-7}$$

$$\text{del2} := \frac{K_{23}(3.) - .0370570745}{.0370570745} \quad \text{del2} = -5.7495124 \cdot 10^{-7}$$

### Flux through HXDS detector Aperture

Now we calculate how much of the emerging spectrum passes through the circular aperture of our detector. In order to do this calculation, we need the expression for the angular distribution of the radiation, and we need to integrate it over the aperture.

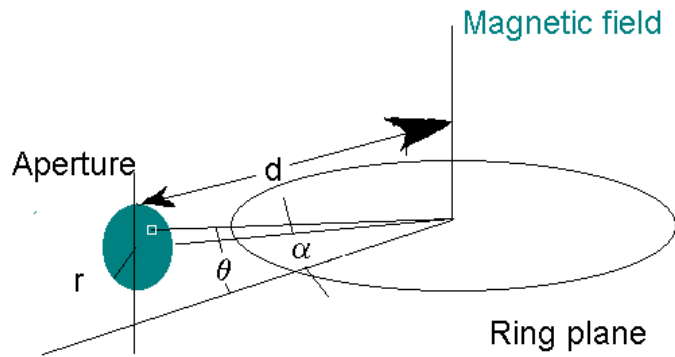
We define

$\alpha$  to be the angle between the detector normal and the orbit plane, assuming the detector normal is always parallel to the ring plane, but the detector can be translated out of the ring plane, so  $\alpha$  measures how far out of plane the detector is translated.

$r$  to be the radius of the circular detector aperture.

$d$  to be the distance from the ring tangent point to the detector aperture.

$\theta$  to be the angle between the orbit plane and the view angle



The storage ring electrons have  $\gamma_0$  as follows where  $E_0$  is their total energy:

$$\gamma_0(E_0) = \frac{E_0}{m \cdot c^2} \quad m \cdot c^2 = 0.5109991 \cdot \text{MeV} \quad \gamma_0(E_0) := \frac{E_0}{0.5109991 \cdot \text{MeV}}$$

and a typical BESSY value might be:  $\gamma_0(797.6 \cdot \text{MeV}) = 1560.86$

### Gyration radius of the electrons

In a field  $H$ , to find the gyroradius, consider an electron of energy  $E_0$  and relativistic factor  $\gamma_0(E_0)$  moving in a circle whose plane is perpendicular to the magnetic field. In one turn, the time is the inverse of the gyration frequency  $\nu$ . The distance travelled in one orbit is  $2\pi\rho$ . The distance is also velocity times time or velocity divided by orbit frequency =  $\beta c/\nu$ . Solving for  $\rho$ ,

$$2 \cdot \pi \cdot \rho \cdot \nu_{\text{gy}}(\gamma, H) = \frac{\beta(\gamma) \cdot c}{\nu_{\text{gy}}(H, \gamma)} \quad \beta(\gamma) = \sqrt{1 - \frac{1}{\gamma^2}}$$

From Jackson, op cit eq. 7.99, adding relativistic mass:

$$\omega_{\text{gy}}(B, \gamma) = 2 \cdot \pi \cdot \nu_{\text{gy}}(B, \gamma) = \frac{e}{(\gamma \cdot m) \cdot c} \cdot B \quad \text{and since in gaussian units, } \mu_0 = 1, H=B.$$

$$\rho_{\text{gy}}(\gamma, H) = \frac{\sqrt{1 - \frac{1}{\gamma^2}} \cdot c}{2 \cdot \pi \cdot \left( \frac{e}{2 \cdot \pi \cdot m \cdot c} \cdot \gamma \right)} \quad \rho_{\text{gy}}(\gamma, H) = \sqrt{\gamma^2 - 1} \cdot \frac{m \cdot c^2}{e \cdot H}$$

Or expressing as a function of  $E_0$ ,

$$\rho_{\text{gy}}(E_0, H) = \sqrt{\gamma_0(E_0)^2 - 1} \cdot \frac{m \cdot c^2}{e \cdot H} = \frac{E_0}{e \cdot H} \cdot \sqrt{1 - \left( \frac{m \cdot c^2}{E_0} \right)^2}$$

If we make a series expansion of the radical:

$$\rho_{\text{gy}}(E_0, H) = \frac{E_0}{e \cdot H} \left[ 1 - \frac{1}{2} \cdot \left( \frac{m \cdot c^2}{E_0} \right)^2 - \left[ \frac{1}{8} \cdot \left( \frac{m \cdot c^2}{E_0} \right)^2 \right]^2 - \dots \right]$$

and 
$$\left( \frac{m \cdot c^2}{797.6 \cdot \text{MeV}} \right)^2 = 4.1 \cdot 10^{-7}$$

we see that even the first order term contributes  $< 10^{-6}$  at our energy, so

$$\rho_{\text{gy}}(E_0, H) := \frac{E_0}{e \cdot H}$$

## The differential photon spectrum

Using Jackson' s eqn 14.80, we first define the parameter  $\xi$ , where  $\varepsilon$  is the x-ray energy:

$$\xi(\varepsilon, H, E_0, \theta) = \frac{2 \cdot \pi \cdot \varepsilon \cdot \rho_{\text{gy}}(E_0, H)}{3 \cdot h \cdot c} \cdot \left( \frac{1}{\gamma_0(E_0)^2} + \theta^2 \right)^{\frac{3}{2}} = \frac{2 \cdot \pi \cdot \varepsilon \cdot E_0}{3 \cdot h \cdot c \cdot e \cdot H} \cdot \left( \frac{1}{\gamma_0(E_0)^2} + \theta^2 \right)^{\frac{3}{2}}$$

$$\frac{2 \cdot \pi}{3 \cdot h \cdot c \cdot e} = 5.6348049 \cdot 10^6 \frac{\text{tesla}}{\text{MeV} \cdot \text{keV}}$$

$$\xi(\varepsilon, H, E_0, \theta) := 5.6348049 \cdot 10^6 \cdot \frac{\varepsilon \cdot E_0}{H} \cdot \left( \frac{1}{\gamma_0(E_0)^2} + \theta^2 \right)^{\frac{3}{2}} \cdot \frac{\text{tesla}}{\text{keV} \cdot \text{MeV}}$$

$$\xi(\text{keV}, 1.5 \cdot \text{tesla}, 797.6 \cdot \text{MeV}, 0) = 0.787912$$

Then, to get the differential photon spectrum, we use Jackson' s eqn 14.83 for the energy radiated per unit frequency interval  $d\omega$  from a single particle into a solid angle  $d\Omega$  from a single pass of an electron :

$$dI(\omega, \gamma, \theta, \xi) = \frac{e^2}{3 \cdot \pi^2 \cdot c} \cdot (\omega \cdot \rho_{\text{gy}})^2 \cdot \left( \frac{1}{\gamma^2} + \theta^2 \right)^2 \cdot \left[ K_{23}(\xi)^2 + \left[ \frac{1}{1 + \frac{1}{(\gamma \cdot \theta)^2}} \right] \cdot K_{13}(\xi)^2 \right] \cdot d\Omega \cdot d\omega$$

Now for the radiated power from a number of electrons passing per unit time,

$$\frac{d}{dt} \varepsilon = dI \cdot (\text{number\_of\_electrons\_passing\_per\_unit\_time}) = dI \cdot \frac{\text{amps}}{e}$$

Also,  $d\omega = \frac{2 \cdot \pi}{h} \cdot d\varepsilon$  which gives



$$\frac{d}{dt}\varepsilon(\text{amps}, \varepsilon, H, E_0, \theta) = \frac{2 \cdot \pi \cdot \text{amps} \cdot e \cdot \left(2 \cdot \pi \cdot \frac{\varepsilon}{h} \cdot \rho_{\text{gy}}(E_0, H)\right)^2}{3 \cdot \pi^2 \cdot c^3 \cdot h} \cdot \left(\frac{1}{\gamma(E_0)^2} + \theta^2\right)^2$$

$$\times \left[ K_{23}(\xi)^2 + \left[ \frac{1}{1 + \frac{1}{(\gamma \cdot \theta)^2}} \right] \cdot K_{13}(\xi)^2 \right] \cdot d\Omega \cdot d\varepsilon$$

Now since  $d\Omega = \cos(\theta) \cdot d\theta \cdot d\phi$

and  $\theta$  is very small,  $< 0.15$  mrad, and  $r/d$  and  $\alpha/d$  are also very small, we integrate over the circular aperture and divide by  $\varepsilon$  to get the expression for a photon spectrum. If we define  $\text{dphperkeV} = \text{factor1} \cdot \text{factor2}$ , with:

$$\text{factor1}(\text{amps}, E_0, H, \varepsilon) = \frac{\left[ (16 \cdot \pi \cdot e \cdot \text{amps}) \left( \rho_{\text{gy}}(E_0, H) \right)^2 \right] \varepsilon}{3 \cdot (h \cdot c)^3}$$

then the photon spectrum is

$$\text{dphperkeV}(\text{amps}, \varepsilon, H, E_0, \alpha, r, d) = \text{factor1}(\text{amps}, E_0, H, \varepsilon) \cdot \text{factor2}(\alpha, r, d, E_0, \varepsilon, H)$$

Now to substitute expressions, evaluate the constants and establish units,

$$\frac{16 \cdot \pi \cdot e \cdot \text{amps} \cdot \rho_{\text{gy}}(E_0, H)^2 \cdot \varepsilon}{3 \cdot (h \cdot c)^3} = \frac{16 \cdot \pi \cdot \text{amps} \cdot E_0^2 \cdot \varepsilon}{3 \cdot e \cdot (h \cdot c)^3 \cdot H^2}$$

$$\frac{16 \cdot \pi}{3 \cdot e \cdot (h \cdot c)^3} = 8.7915208 \cdot 10^{29} \frac{\text{Hz}}{\text{keV}} \cdot \frac{\text{tesla}^2}{\text{amp} \cdot \text{MeV}^2 \cdot \text{keV}}$$

giving the formula for factor1, in which arguments are substituted in with physical units and are evaluated with units. Note: from this point on, Mathcad notation is used. Wherever you see ":", that is an active declaration used in subsequent calculations. Also, Mathcad has some specific nomenclature for indicating a quantity to a power. For example  $f(x)$  to the second power is written  $f(x)^2$  in Mathcad notation.

$$\text{factor1}(\text{amps}, \varepsilon, E_0, H) := (8.7915208 \cdot 10^{29}) \cdot \left( \frac{\text{Hz}}{\text{keV}} \cdot \frac{\text{tesla}^2}{\text{amp} \cdot \text{MeV}^2 \cdot \text{keV}} \right) \cdot \text{amps} \cdot \varepsilon \cdot \left( \frac{E_0}{H} \right)^2$$

$$\text{factor3}(\varepsilon, H, E_0, \theta) := \left[ \left( K_{23}(\xi(\varepsilon, H, E_0, \theta)) \right)^2 \dots \right. \\ \left. + \left[ \frac{\theta^2}{\theta^2 + \frac{1}{\gamma_0(E_0)^2}} \right] \cdot \left( K_{13}(\xi(\varepsilon, H, E_0, \theta)) \right)^2 \right]$$

$$\text{factor2}(\alpha, r, d, E_0, \epsilon, H) := \int_{\alpha - \frac{r}{d}}^{\alpha + \frac{r}{d}} \sqrt{\left(\frac{r}{d}\right)^2 - (\theta - \alpha)^2} \cdot \left(\frac{1}{\gamma_0(E_0)^2 + \theta^2}\right)^2 \cdot \text{factor3}(\epsilon, H, E_0, \theta) d\theta$$

$$\text{dphperkeV}(\text{amps}, \epsilon, H, E_0, \alpha, r, d) := \text{factor1}(\text{amps}, \epsilon, E_0, H) \cdot \text{factor2}(\alpha, r, d, E_0, \epsilon, H)$$

Next, we evaluate dphperkeV for a set of energies  $\epsilon_i$ , and for 5 electrons in the ring, and a particular set of  $H_1$ ,  $E_1$ ,  $\theta$  ( $=0$ ),  $r=2.5$  and  $d_1$  corresponding to run #500480d1i0 of the ssd\_x on the PTB white beam line at BESSY.

$$E_1 := 798.191 \cdot \text{MeV} \quad i_1 := (5) \cdot 7.6 \cdot 10^{-13} \cdot \text{amp} \quad H_1 := 1.490797 \cdot \text{tesla}$$

$$d_1 := 16169.48$$

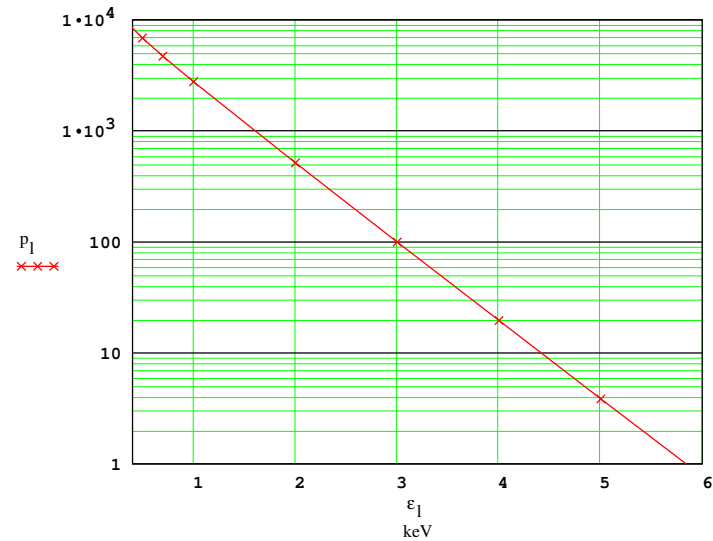
$$l := 0..11$$

$$\epsilon_i :=$$

- |    |
|----|
| .1 |
| .3 |
| .5 |
| .7 |
| 1  |
| 2  |
| 3  |
| 4  |
| 5  |
| 6  |
| 7  |
| 10 |

Now we form the quantity  $p_1$ , which must be dimensionless for plotting purposes:

$$p_1 := \text{dphperkeV}(i_1, \epsilon_i \cdot \text{keV}, H_1, E_1, 0., 2.5, d_1) \cdot \frac{\text{keV}}{\text{Hz}}$$



Differential photon spectrum from BESSY

Notice that the spectrum is very steep. If the energy of the electrons in the storage ring were higher, the spectrum would be flatter. For our measurements, this means that to detect photons above ~ 2 keV, we must get rid of great many low energy photons if we are to avoid clogging up our detector with them.

### Variation of flux through aperture with detector displacement

As the detector is moved in the vertical direction, out of the storage ring plane, the intensity of the synchrotron x-radiation varies as shown below. This means that the detector must be carefully aligned so that the aperture is centered on the ring plane.

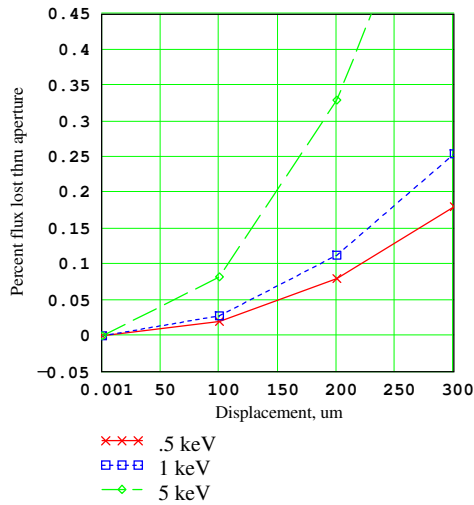
m := 0..3

ds<sub>m</sub> :=

.0005
.1
.2
.3

$$\text{norm}_1 := \text{dphperkeV}\left(i_1, \epsilon_1 \cdot \text{keV}, H_1, E_1, \frac{ds_0}{d_1}, 2.5, d_1\right)$$

$$q_{m,1} := \frac{\text{dphperkeV}\left(i_1, \epsilon_1 \cdot \text{keV}, H_1, E_1, \frac{ds_m}{d_1}, 2.5, d_1\right)}{\text{norm}_1}$$



π

This result shows that the aperture must be aligned to better than 100 μm.


### Numerical integration of photons incident on crystal:

Computational detail: the numerical integral ends up with an extremely small imaginary part, of order 10<sup>-40</sup>, so we take the real part:

$$\text{ssdInt}\left(\text{amps}, H, E_0, \alpha, r, d\right) := \int_{0.30789 \cdot \text{keV}}^{10 \cdot \text{keV}} \text{Re}\left(\text{dphperkeV}\left(\text{amps}, \epsilon, H, E_0, \alpha, r, d\right)\right) d\epsilon$$

$$\text{ssdInt}\left(i_1, H_1, E_1, 0, 2.5, d_1\right) = \text{Hz}$$

This number represents the total photons incident on the detector. Many of them will be absorbed in the detector windows. That will be accounted for in the SYNCH model, which calculates the photoelectric absorption from the windows using Henke tables.

 Reference: C:\WINMCAD\Units.mcd

See <http://hea-www.harvard.edu/MST/hxds/topics/units.ps>

The above derivation needs to be checked against the PTB calculation. The algorithm was coded into FORTRAN for use in fitting white beam BESSY pulse height spectra from the SSD and FPC detectors.

#### 4.6.2 The SYNCH Model

The synchrotron algorithm derived in §4.6.1 was coded in FORTRAN as an XSPEC local model, named SYNCH. This model calculates the photon flux output from a synchrotron over a circular aperture, including the damping effect of six filters, and passes the resulting spectrum to XSPEC to be folded with the detector response matrix. Since the filter calculations are done by calling the JMKMOD subroutine “source,” the SYNCH model is limited to only 1024 channels (maximum array dimensions within subroutine source), and a response matrix of size 1024 x 1024. The model has provisions for adding Gaussian lines to the spectrum and also for pileup calculations. The pileup calculation at present is based on a very simple algorithm that piles up every channel in the synchrotron spectrum with all the other channels in the spectrum. A more realistic algorithm is needed for a better analysis of the pileup features. The input parameters of the model are self-explanatory and are well documented within the code. One, however, should note that the ring current is either provided directly by the “current” parameter (when number of electrons = 0) or calculated from the number of electrons (when number of electrons is nonzero).

#### 4.6.3 Synchrotron Measurement Procedures

The procedure for measuring the undispersed synchrotron radiation involved injecting the storage ring with approximately 2 mAmps of current and allowing 2 hours for the beam to stabilize. After this waiting time, an RF signal was injected perpendicular to the electron beam. This RF wave as scanned in frequency until a resonance with the electrons in the storage ring was obtained. This could be observed by measuring a sharp decrease in the ring current as the excitation caused the electrons to depart from their orbit and collide with the walls of the storage ring.

Reaching this resonance meant that the resonant frequency, and therefore the energy, of the electrons had been reached. Once the energy of the electrons was measured and the orbit of the electrons in the storage ring had become stable, a polarizing crystal was inserted in the beam line. This crystal was scanned in the vertical direction until a peak in counting rate was reached. This provided information on exactly where the electron beam was in the storage ring. Knowing this, it then possible to scan the detector in the vertical plane so as to make it lie in the same plane as the electron orbit.

Next the ring current was reduced by slowly inserting a baffle into the storage ring which ejected some fraction of the electrons on each orbit until the desired ring current was reached. During this reduction of current, the current was measured using a calibrated photodiode in the SX700 beam line. Once the ring current got below 1000 electrons it was possible to see the quantum jumps in the ring current as single electrons were removed from the storage ring.

The spectral output from BESSY is peaked at low energy. With the Aluminum IR shield in place, the peak corresponds to about 1 keV. As a consequence, the usable photon flux tends to tail out around 4-5 keV. In order to achieve significant counting statistics at the higher energies desired (up to 10 keV), Aluminum filters were placed into the aperture that could suppress the lower energy photons, allowing a higher ring current and therefore a higher rate of high-energy photons. The two filters used were a 27.4  $\mu\text{m}$  and a 133.4  $\mu\text{m}$  Al filter. The 27.4  $\mu\text{m}$  filter effectively shifted the peak energy synchrotron source spectrum to 4 keV, while the 133.4  $\mu\text{m}$  filter shifted it even farther to 6 keV. As can be seen in Figure 4.12, there is now sufficient flux at 10 keV to be useful in fitting.

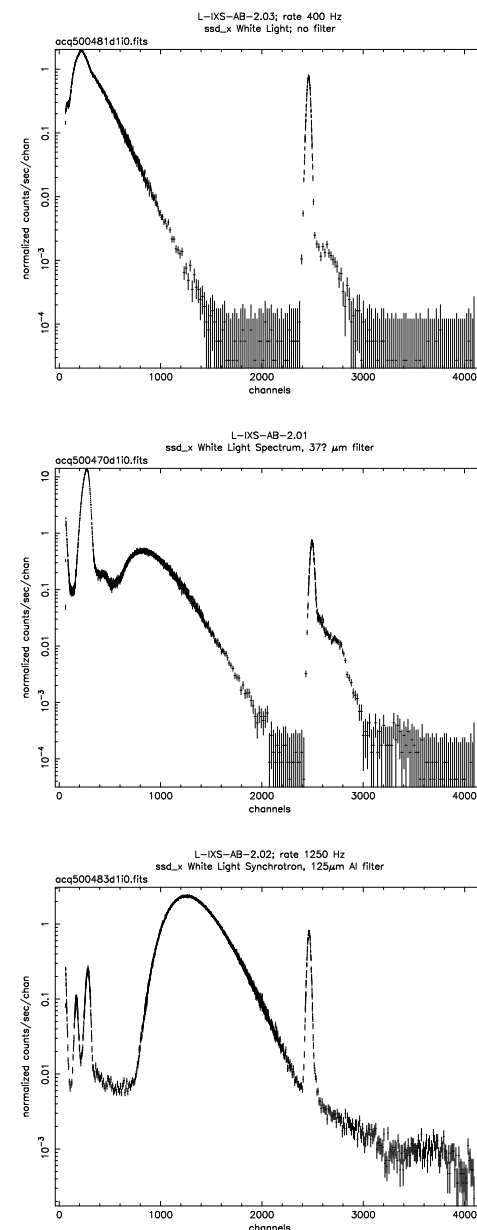


Figure 4.12: *ssd\_x* Synchrotron White Light Spectra

Energy (keV)	Transmission	Al thickness $\mu\text{mm}$
2.5	$9.11 \times 10^5$	27.0
3.	$3.41 \times 10^3$	27.0
4.	$7.48 \times 10^2$	27.4
5.	$2.49 \times 10^1$	27.6
6.	$4.28 \times 10^1$	27.7
7.	$5.94 \times 10^1$	27.4
4.5	$1.23 \times 10^4$	132.5
5.	$1.29 \times 10^3$	132.3
5.5	$6.02 \times 10^3$	133.6
6.	$1.90 \times 10^2$	133.2
6.5	$4.24 \times 10^2$	134.
7.	$7.77 \times 10^2$	134.4

Table 4.10: Thicknesses of SSD Al filter material, measured at NSLS.

This technique was regarded as somewhat speculative, because the great attenuation of the thick Al filters would have to be corrected to a fraction of 1% in order to make the measurement useful. However, we did a careful measurement of the x-ray absorption of this thick Al filter material at the BNL synchrotron, in order to aid the measurement. The net result was an equivalent thicknesses of  $27.4 \pm 0.3 \mu\text{m}$  and  $133.4 \pm 0.8 \mu\text{m}$ . See Table 4.10 for the complete set of BNL measurements.

The development in §4.6.1 was coded into FORTRAN, and implemented as the XSPEC model subroutine SYNCH. Using the response matrices derived above (from the BESSY monochromator spectral response function tests), we can then fit the spectra. If all goes well, the normalization factor should be unity; i.e. the absolute intensity of the synchrotron light beam should be computed correctly and require no renormalization in order to match the data.

#### 4.6.4 Results of the Fitting

The first case is shown in Figure 4.13. Here, we see the results of fitting to the data from the `ssd_5`.

The upper panel shows the fit to the entire pulse height spectrum, from 0.4–6.5 keV. The fit is good at energies above 2 keV. It is not too bad qualitatively down to about 0.8 keV, but the residuals show considerable structure. The SYNCH model in XSPEC used here contains the synchrotron continuum and a Henke model of absorption by the filters. This has the limitation that the fine structure from EXAFS at the O-K, Ge-L and Al-K edges known to exist are not in the Henke data. The correct way to do this is to include a `.arf` auxiliary response file in the XSPEC fit, with the `.arf` file containing the QE vs. E information discussed in §4.5. Since we have not yet finalized those QE values, this remains to be done. Therefore, to obtain the best present value of the broadband QE, we restrict ourselves to data at higher energy, where the window absorption is less important.

The parameters for this fit are listed in Table 4.11. The lower panel in Figure 4.13 shows the fit including the energy range 3.5–6.6 keV only. The parameters for this fit are listed in Table 4.12. The overall normalization, parameter ‘norm’ is consistent with 1.00, indicating that the high energy QE is 100%.

The second case is shown in Figure 4.14. Here, we see the results of fitting to the data from the `ssd_x`. The upper panel shows the fit to the entire pulse height spectrum. Structure in the

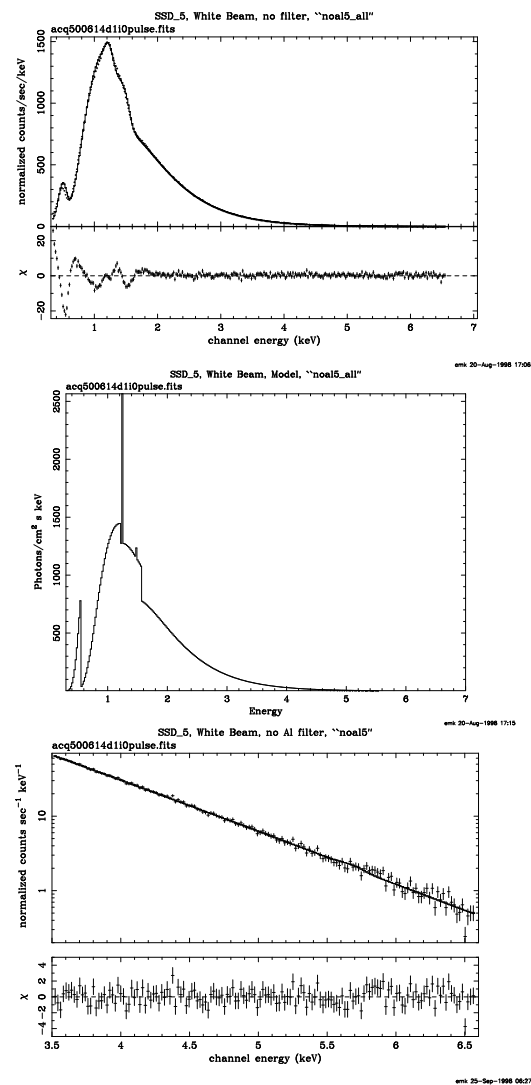


Figure 4.13: Data and XSPEC fit at the white beam for `ssd_5` with no Al filter, with input synchrotron model folded through XSPEC. The upper panel shows the entire pulse height distribution and the XSPEC calculation, with residuals, from the lower level discriminator cutoff at 0.4–.5 keV. The center panel shows just the input synchrotron+window absorption model, SYNCH, from 0.4–6.5 keV. The lower panel shows the pulse height distribution and the folded model with residuals, for 3.5–6.6 keV only.

Parameter	Value	Status
alpha	0.	frozen
radius	2.500	frozen
distance	1.6242E+04	frozen
E_electr	798.2	frozen
H	1.491	frozen
e_to_cur	7.6970E-13	frozen
N_electr	8.000	frozen
current	3.800	frozen
pileup	0.	frozen
filter1	2.000	frozen
thcknss1	3.1241E-05	frozen
filter2	6.000	frozen
thcknss2	5.7040E-05	frozen
filter3	32.00	frozen
thcknss3	3.5067E-06	frozen
filter4	48.00	frozen
thcknss4	2.9854E-04	frozen
filter5	19.00	frozen
thcknss5	0.	frozen
filter6	45.00	frozen
thcknss6	0.	frozen
lineE1	1.239	frozen
sigma1	1.9814E-03	frozen
norm1	237.3	frozen
lineE2	1.486	frozen
sigma2	4.3000E-04	frozen
norm2	0.3809	frozen
lineE3	1.557	frozen
sigma3	8.0000E-03	frozen
norm3	3.5012E-07	frozen
norm	0.9719	0.2041E-02

Table 4.11: Fitting parameters for `ssd_5` white beam run, all energies, no Al filter. Runid 500614, channels = 141 - 299, nbins = 159, reduced  $\chi^2 = 0.9954577$

Parameter	Value	Status
alpha	0.	frozen
radius	2.500	frozen
distance	1.6242E+04	frozen
E_electr	798.2	frozen
H	1.491	frozen
e_to_cur	7.6970E-13	frozen
N_electr	8.000	frozen
current	3.800	frozen
pileup	0.	frozen
filter1	2.000	frozen
thcknss1	5.3860E-05	0.1252E-04
filter2	6.000	frozen
thcknss2	5.7279E-05	frozen
filter3	32.00	frozen
thcknss3	3.0000E-06	frozen
filter4	48.00	frozen
thcknss4	2.9745E-04	frozen
filter5	19.00	frozen
thcknss5	0.	frozen
filter6	45.00	frozen
thcknss6	0.	frozen
lineE1	1.240	frozen
sigma1	1.0000E-03	frozen
norm1	20.00	frozen
norm	1.019	0.1270E-01

Table 4.12: Fitting parameters for `ssd_5` white beam run, only high energy, no Al filter. Runid 500614, channels 176-329, nbins=154, reduced  $\chi^2 = 0.9547486$

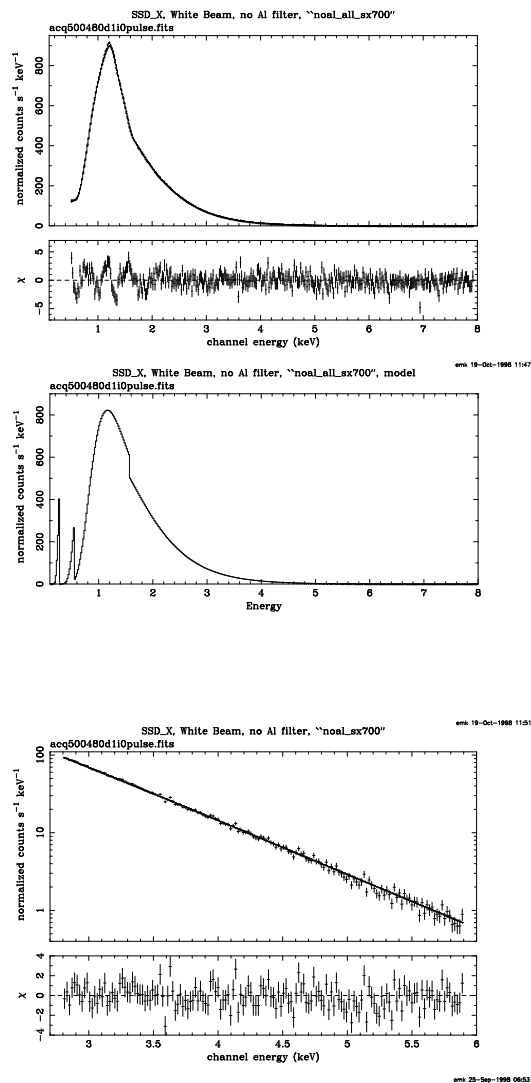


Figure 4.14: Data and XSPEC fit at the white beam for *ssd\_x* with no Al filter. The upper panel shows 0.4–7.9 keV, with input SYNCH model folded through XSPEC, and residuals. The center panel shows the input synchrotron+window absorption SYNCH model. The lower panel shows just 2.8–5.9 keV, with folded model.

fit is very similar to that for Figure 4.13 for the same reasons. The parameters for this fit are listed in Table 4.13. The middle panel shows the input model before being folded through the detector response by XSPEC. The absorption edges from C–K at 0.28 keV, O–K at 0.54 keV and Al–K at 1.58 keV are seen, as well as the general absorption that causes the smooth synchrotron spectrum to turn over at energies below 1.5 keV. The lower panel again shows the fit to the higher energies, with residuals showing no structure or energy dependence. The parameters for this fit are listed in Table 4.14. The absence of structure or energy dependence is significant because the overall normalization for the *ssd\_x* is not consistent with 1.00, rather being about 27% low. Lack of structure in the residuals means that whatever is affecting the normalization is independent of energy, so must be some sort of beam blocking, rather than an error in the energy scale or in the energy-dependent part of the prediction calculation.

Whatever is causing this discrepancy for *ssd\_x* is not a function of energy. Other comparisons of *ssd\_x* and *ssd\_5* do not show this discrepancy. See Zhao et al. (1998). Also compare the narrow band QE measurements discussed in §4.5. Therefore, our present conclusion is that the *ssd\_5* QE normalization is 100%, and that we do not have a corresponding number for *ssd\_x* from the white beam calibrations.

Figure 4.15 shows the response of *ssd\_5* to the white beam, with a 27.4  $\mu\text{m}$  filter. In the upper panel, we see a large peak at 1.5 keV. This is the synchrotron continuum being transmitted through the Al filter just below its Al–K edge. In the upper panel, at energies below  $\sim 0.8$  keV, we see the shelf discussed previously. Here, the calculated shelf is far less intense than the observed one. In the region from 1.8–2.5 keV we see interpeak events from electronic pileup, as discussed previously. From  $\sim 2.8$ –3.1 keV, we see an apparent pileup peak. The observed peak is not at the same pulse height as the calculated one. We think we know the defect in the algorithm that causes this, but have not fixed it yet. At  $E > 3.3$  keV, the fit is rather good. The parameters for this fit are listed in Table 4.15. The overall normalization, our main interest here, is not very reliable in this fit; see next fit.

The lower panel in Figure 4.15 shows the fit restricted to 3.5–6.5 keV. The residuals show little structure. There is a feature in the folded model curve at 5.7 keV that causes a peak in the residuals. This is probably in the response matrix, where the upper boundary of the measured response curve meets the extrapolation of the matrix to higher energies, where we have no measurements on which to base the matrix. The overall normalization for this fit, listed as ‘norm’ in Table 4.16, is far from 1.00. We do not understand why this is so, but we realize from Table 4.10 that the attenuation in this filter at 4 keV is about a factor of 13.5. One possible cause of discrepancy is that the thickness derived from the NSLS x-ray transmission measurements was measured just on one spot in the Al foil, used later to fabricate the filters by cutting out small circular disks for each detector. Therefore, if there was any thickness variation in the foil sheet, the actual sample use in the detector could have a different thickness. However, when we allowed the thickness of the Al foil to vary as a free parameter in the XSPEC fits, the result was consistent with the nominal value from NSLS.

Figure 4.16 shows the response of *ssd\_x* to the white beam, with a 27.4  $\mu\text{m}$  filter. In the upper panel, the energy range is 0.8–5.9 keV. We again see a large peak at 1.5 keV, from the Al–K absorption edge. The residuals in the vicinity of the energy of that peak are qualitatively different from those for *ssd\_5* (Figure 4.15), and that may be due to differences in the faithfulness of the energy scale, which is based on the  $^{244}\text{Cm}$  source for the *ssd\_5*, but for the *ssd\_x* must rely on less direct means. The interpeak pileup between 1.6–3.0 keV is also different. The lower panel shows the fit for the higher energy range, 3.2–9.8 keV. There is some structure in the residuals. This may indicate an inability to fit the shape of the Al photoelectric absorption vs. energy. That in turn could be due to limitations in our rather simple pileup correction model. The value for ‘norm’, the last entry in Table 4.18, is far from 1.00, as it was for the *ssd\_5* with the 27.4  $\mu\text{m}$  Al filter.

Parameter	Value	Status
alpha	0.	frozen
radius	2.500	frozen
distance	1.6242E+04	frozen
E_electr	798.7	frozen
H	1.491	frozen
e_to_cur	7.6970E-13	frozen
N_electr	5.000	frozen
current	3.800	frozen
pileup	0.	frozen
filter1	2.000	frozen
thcknss1	1.7730E-05	0.9757E-06
filter2	6.000	frozen
thcknss2	8.6098E-05	0.1066E-05
filter3	32.00	frozen
thcknss3	0.	frozen
filter4	48.00	frozen
thcknss4	2.5155E-04	0.5297E-01
filter5	19.00	frozen
thcknss5	0.	frozen
filter6	45.00	frozen
thcknss6	0.	frozen
lineE1	0.6148	0.1370
sigma1	0.3954	0.5217E-01
norm1	17.53	7.100
lineE2	0.9653	0.6952
sigma2	0.9194	0.2023
norm2	3.389	2.873
norm	0.7178	0.6949E-02

Table 4.13: Fitting parameters for `ssd_x` white beam, all energies, no Al filter. Runid 500480, channels 20–400, nbins=381, reduced  $\chi^2 = 1.648170$

Parameter	Value	Status
alpha	0.	frozen
radius	2.500	frozen
distance	1.6242E+04	frozen
E_electr	798.7	frozen
H	1.491	frozen
e_to_cur	7.6970E-13	frozen
N_electr	5.000	frozen
current	3.800	frozen
pileup	0.	frozen
filter1	2.000	frozen
thcknss1	1.9764E-05	frozen
filter2	6.000	frozen
thcknss2	2.0924E-05	frozen
filter3	32.00	frozen
thcknss3	0.	frozen
filter4	48.00	frozen
thcknss4	6.3292E-05	0.8126E-04
filter5	19.00	frozen
thcknss5	3.6279E-05	frozen
filter6	45.00	frozen
thcknss6	0.	frozen
lineE1	1.225	frozen
sigma1	2.9965E-02	frozen
norm1	1.219	frozen
lineE2	1.109	frozen
sigma2	0.2560	frozen
norm2	2.343	frozen
norm	0.7329	0.6280E-02

Table 4.14: Fitting parameters for `ssd_x` white beam, only high energies, no Al filter. Runid 500480, channels 138–296, nbins=159, reduced  $\chi^2 = 1.205958$



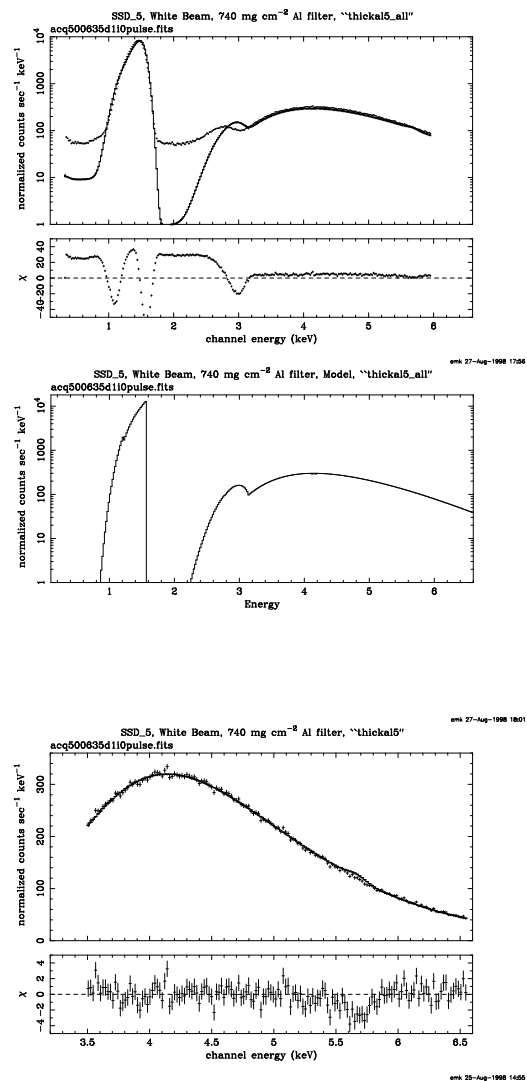


Figure 4.15: Data and XSPEC fit for *ssd\_5* at the white beam with  $27.4 \mu\text{m}$  Al filter. The upper panel shows the entire pulse height distribution, 0.4–6.0 keV, with SYNCH/XSPEC model. The center panel shows the input SYNCH model, 0.4–6.0 keV. The lower panel shows 3.5–6.5 keV, with folded model.

Parameter	Value	Status
alpha	0.	frozen
radius	2.500	frozen
distance	1.6242E+04	frozen
E_electr	798.2	frozen
H	1.491	frozen
e_to_cur	7.6970E-13	frozen
N_electr	0.	frozen
current	1403.	frozen
pileup	2.2067E-02	0.1473E-03
filter1	2.000	frozen
thcknss1	2.7400E-03	frozen
filter2	6.000	frozen
thcknss2	0.	frozen
filter3	32.00	frozen
thcknss3	9.7414E-06	0.5422E-07
filter4	48.00	frozen
thcknss4	0.	frozen
filter5	19.00	frozen
thcknss5	0.	frozen
filter6	45.00	frozen
thcknss6	0.	frozen
norm	0.5531	0.8266E-03

Table 4.15: Fitting parameters for *ssd\_5* white beam, all energies with  $27.4 \mu\text{m}$  Al filter. Runid 500635, channels 16-299, nbins=284, reduced  $\chi^2 = 353.4951$

Parameter	Value	Status
alpha	0.	frozen
radius	2.500	frozen
distance	1.6242E+04	frozen
E_electr	798.2	frozen
H	1.491	frozen
e_to_cur	7.6970E-13	frozen
N_electr	0.	frozen
current	1403.	frozen
pileup	2.4664E-02	0.3252E-01
filter1	2.000	frozen
thcknss1	2.7400E-03	frozen
filter2	6.000	frozen
thcknss2	5.6046E-11	0.2073
filter3	32.00	frozen
thcknss3	1.4657E-05	0.5497E-03
filter4	48.00	frozen
thcknss4	7.9732E-07	0.2386
filter5	19.00	frozen
thcknss5	7.5167E-10	0.3916
filter6	45.00	frozen
thcknss6	0.	frozen
norm	0.5984	0.1145E-01

Table 4.16: Fitting parameters for *ssd\_5* white beam, Higher energies with  $27.4 \mu\text{m}$  Al filter. Rumid 500635, channels 176-329, nbins=154, reduced  $\chi^2 = 1.577946$

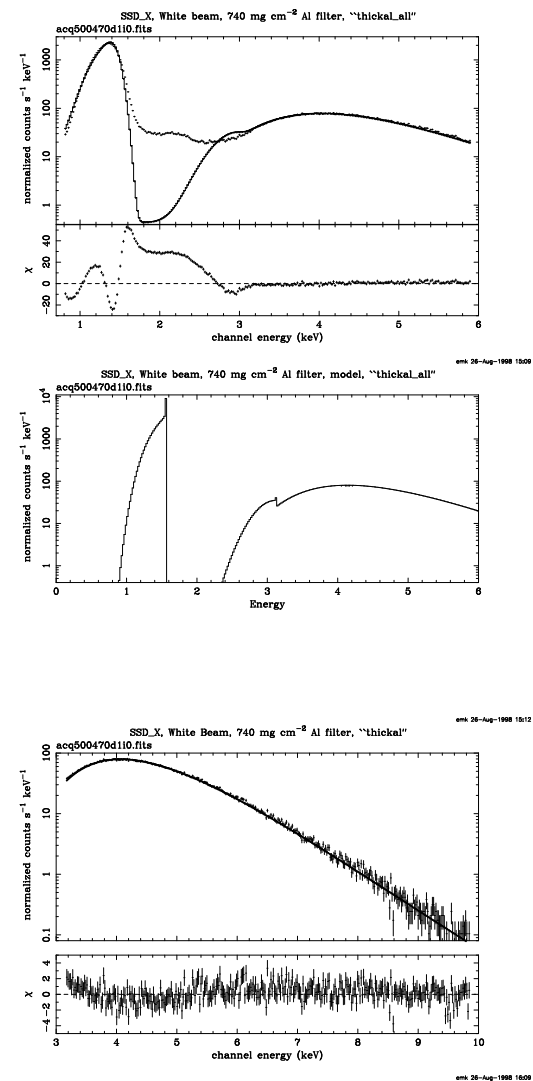


Figure 4.16: Data and XSPEC fit for *ssd\_x* at the white beam with  $27.4 \mu\text{m}$  Al filter. The upper panel shows 0.4–6.0 keV, with SYNCH/XSPEC folded model. The parameters for this fit are listed in Table 4.17. The center panel shows the input SYNCH model, 0.4–6.0 keV. The lower panel shows 3.5–6.6 keV, with folded model.

Parameter	Value	Status
alpha	0.	frozen
radius	2.500	frozen
distance	1.6242E+04	frozen
E_electr	798.7	frozen
H	1.491	frozen
e_to_cur	7.6970E-13	frozen
N_electr	438.0	frozen
current	3.800	frozen
pileup	9.2580E-03	frozen
filter1	2.000	frozen
thcknss1	2.7400E-03	frozen
filter2	6.000	frozen
thcknss2	0.	frozen
filter3	32.00	frozen
thcknss3	0.	frozen
filter4	48.00	frozen
thcknss4	2.7472E-04	frozen
filter5	19.00	frozen
thcknss5	4.8176E-09	frozen
filter6	45.00	frozen
thcknss6	0.	frozen
lineE2	1.560	0.2529E-02
sigma2	8.0000E-03	frozen
norm2	60.99	0.4718
norm	0.6060	0.9617E-03

Table 4.17: Fitting parameters for `ssd_x` white beam, all energies with 27.4  $\mu\text{m}$  Al filter. Runid 500470, channels 41-299, nbins=259, reduced  $\chi^2 = 236.7270$

Parameter	Value	Status
alpha	0.	frozen
radius	2.500	frozen
distance	1.6242E+04	frozen
E_electr	798.7	frozen
H	1.491	frozen
e_to_cur	7.6970E-13	frozen
N_electr	438.0	frozen
current	3.800	frozen
pileup	3.3334E-04	frozen
filter1	2.000	frozen
thcknss1	2.7400E-03	frozen
filter2	6.000	frozen
thcknss2	0.	frozen
filter3	32.00	frozen
thcknss3	0.	frozen
filter4	48.00	frozen
thcknss4	2.1681E-03	0.1004E-03
filter5	19.00	frozen
thcknss5	1.2500E-04	frozen
filter6	45.00	frozen
thcknss6	0.	frozen
lineE2	1.560	frozen
sigma2	8.0000E-03	frozen
norm2	60.99	frozen
norm	0.6769	0.3091E-02

Table 4.18: Fitting parameters for `ssd_x` white beam, higher energies with 27.4  $\mu\text{m}$  Al filter. Runid 500470, channels 161-500, nbins=340, reduced  $\chi^2 = 1.304896$

Figure 4.17 shows the result of the run taken by exposing `ssd_5` to the white beam, using the  $133.4 \mu\text{m}$  Al filter. In the upper panel, we see the entire energy range from 0.4–10.8 keV. The broad peak at  $\sim 5$  keV is from the synchrotron continuum. It falls off to higher energy because of the falling synchrotron spectrum. It also falls off below 5 keV because of absorption in this very thick Al filter. The shelf from  $\sim 0.4 - 3.7$  keV is caused by incomplete charge collection events from the main peak. There is a peak in the data at about 1.5 keV. This comes from the continuum spectrum being very intense at that energy, and being transmitted partially through the Al filter below its K edge. We were not able to get even a qualitatively satisfactory fit without adding two lines, `lineE1` and `lineE2` in Table 4.19. From Table 4.10 we see that at 6 keV, this filter attenuates by about a factor of fifty. Also, using the Henke tables, Henke et al. (1993), we find an attenuation factor of  $3.15 \times 10^5$  just below the Al–K edge. With such a large factor, we perhaps cannot expect to get an accurate fit across the edge; the discontinuity in the photoelectric cross section of Al may not be well enough known for that. There is also some possibility that some fluorescence Al– $K_\alpha$  radiation is generated within the filter and escapes out its back, into our detector. The calculation also shows a peak at about 1.2 keV. This comes from the response matrix used for the fits, and is meant to account for Ge–L fluorescence from the detector crystal. As a result of observing this, we need to correct the response matrix.

In the lower panel, we show the fit over the 4.8–10.9 keV range. Here, the only peculiarity is the bump in the calculated response at  $\sim 5.65$  keV from the joining of measured to extrapolated response matrix. This region was ignored in the fits that gave the parameters in Table 4.20.

The parameters for the fits in Figure 4.17 are given in Table 4.19 and Table 4.20. The overall normalization, ‘norm’, is far from 1.00. This is perhaps not too surprising, since the attenuation in this very thick Al filter is very large, about a factor of 50 at 6 keV, and we just may not be able to calculate it and correct for it to sufficient accuracy. What are the possible sources of error? First, if we make a small error in the energy scale, since the absorption cross section is varying with the  $8/3$  power of energy, there is a larger error in absorption. For example, a 20 eV 0.3% change in energy gives a 3.5% change in x-ray transmission at 6 keV for this filter. This is not nearly large enough to explain the difference.

Figure 4.18 shows the result of the run taken by exposing `ssd_x` to the white beam, using the  $133.4 \mu\text{m}$  Al filter. In the upper panel, we see the entire energy range from 0.4–11.6 keV. In addition to the main broad peak at 6 keV from the synchrotron continuum plus absorption in the vberly thick Al filter, we see peaks at lower energy. The peak at 1.5 keV is from continuum x-rays penetrating the Al filter just below the Al–K edge. We were not able to get a good fit without adding two lines at 1.486 and 1.550 keV to the model. As in the similar case for `ssd_5`, the model was unable to match the data across the Al–K edge. There is another line in the data, at 0.89 keV. We are not able to identify its source at the present time. The parameters of the fit are given in Table 4.21. The normalization is far from 1.00, but we would use this normalization because of the uncertainties introduced by attempting to fit the low energies.

The lower panel shows the fit over the 3.8–10.6 keV energy range. Here, the low energy features are ignored, and we concentrate on the main peak. The residuals show some structure, which we cannot explain. The parameters of the fit are given in Table 4.22. The normalization is far from 1.00.

The results of all the absolute calibration runs analyzed are shown in Table 4.23. The first column identifies the detector. The second gives a reference to the filename in `/data/axaf/emk/xspec/logs/white` for the XSPEC output files, or indicates a MEAN between two runs. The third column gives the unique HXDS RUNID. The fourth column gives the energy range analyzed. The fifth column gives the “rawQE” derived from the ‘norm’ parameter in the XSPEC output for the run. This has been corrected for dead time by modifying the integration

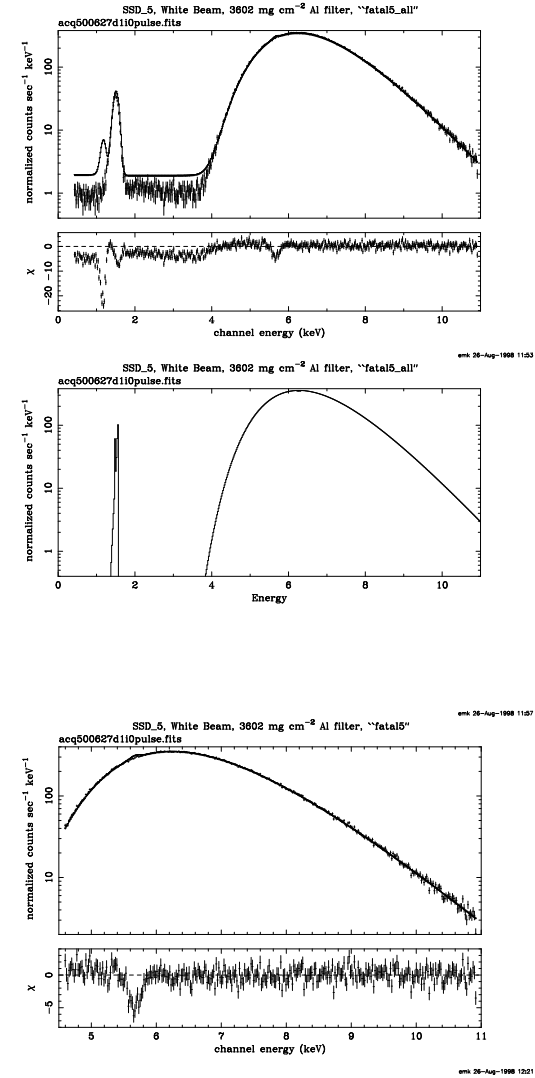


Figure 4.17: Data and XSPEC fit for `ssd_5` at the white beam with  $133.4 \mu\text{m}$  Al filter. The upper panel shows the entire pulse height distribution from the lower level discriminator cutoff at 0.4–10.8 keV, with folded SYNCH/XSPEC model. The center panel shows the input SYNCH model, 0.4–10.8 keV. The lower panel shows 4.8–10.9 keV, with folded model.

Parameter	Value	Status
alpha	0.	frozen
radius	2.500	frozen
distance	1.6242E+04	frozen
E_electr	798.2	frozen
H	1.491	frozen
e_to_cur	7.6970E-13	frozen
N_electr	0.	frozen
current	1.2901E+05	frozen
pileup	9.0914E-05	frozen
filter1	2.000	frozen
thcknss1	1.3340E-02	frozen
filter2	6.000	frozen
thcknss2	4.6609E-06	frozen
filter3	32.00	frozen
thcknss3	0.	frozen
filter4	48.00	frozen
thcknss4	6.8707E-05	frozen
filter5	19.00	frozen
thcknss5	1.0000E-05	frozen
filter6	45.00	frozen
thcknss6	0.	frozen
lineE1	1.550	0.8236E-01
sigma1	8.0000E-03	frozen
norm1	8864.	0.1054E+06
lineE2	1.486	0.4013E-01
sigma2	4.3000E-04	frozen
norm2	3.5642E+05	0.5932E+05
norm	0.6893	0.7891E-03

Table 4.19: Fitting parameters for *ssd\_5* white beam, all energies with 133.4  $\mu\text{m}$  Al filter. Runid 500627, channels 21-549, nbins=529, reduced  $\chi^2 = 12.19044$

Parameter	Value	Status
alpha	0.	frozen
radius	2.500	frozen
distance	1.6242E+04	frozen
E_electr	798.2	frozen
H	1.491	frozen
e_to_cur	7.6970E-13	frozen
N_electr	0.	frozen
current	1.2901E+05	frozen
pileup	4.1963E-06	0.2438E-02
filter1	2.000	frozen
thcknss1	1.3340E-02	frozen
filter2	6.000	frozen
thcknss2	2.3189E-07	0.1104
filter3	32.00	frozen
thcknss3	0.	frozen
filter4	48.00	frozen
thcknss4	1.3648E-07	0.8630E-01
filter5	19.00	frozen
thcknss5	7.4147E-07	0.2029
filter6	45.00	frozen
thcknss6	0.	frozen
lineE1	1.550	frozen
sigma1	8.0000E-03	frozen
norm1	8864.	frozen
lineE2	1.486	frozen
sigma2	4.3000E-04	frozen
norm2	3.5642E+05	frozen
norm	0.7496	0.7787E-02

Table 4.20: Fitting parameters for *ssd\_5* white beam, higher energies with 133.4  $\mu\text{m}$  Al filter. Runid 500627, channels 231-269 and 301-549, nbins=288, reduced  $\chi^2 = 1.164951$

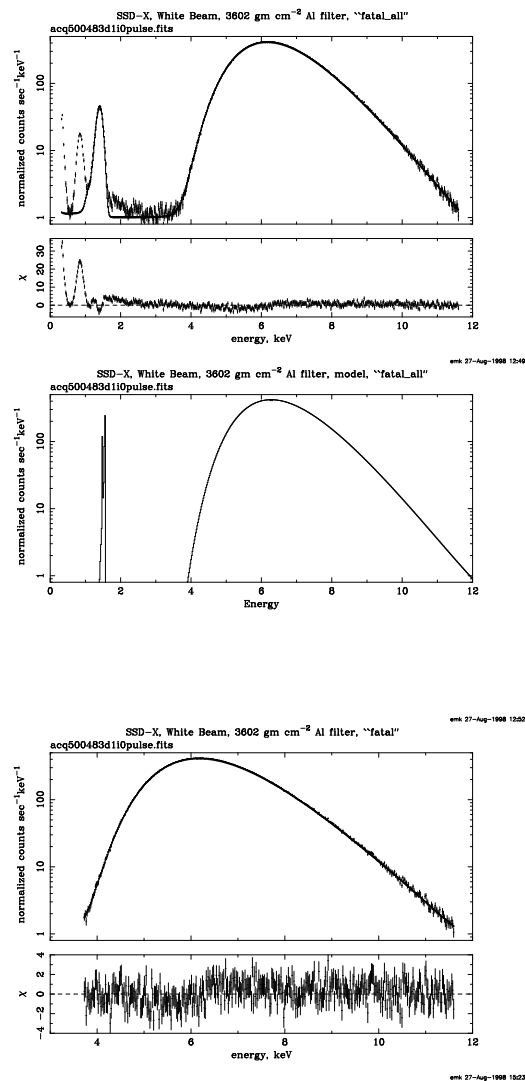


Figure 4.18: Data and XSPEC fit for `ssd_x` at the white beam with  $133.4 \mu\text{m}$  Al filter. The upper panel shows the entire pulse height distribution from the lower level discriminator cutoff at 0.4–11.6 keV, with input synchrotron model folded through XSPEC. The center panel shows the input SYNCH model, 0.4–11.6 keV. The lower panel shows just 3.8–10.6 keV, with folded model.

Parameter	Value	Status
alpha	0.	frozen
radius	2.500	frozen
distance	1.6242E+04	frozen
E_electr	798.2	frozen
H	1.491	frozen
e_to_cur	7.6970E-13	frozen
N_electr	0.	frozen
current	1.2901E+05	frozen
pileup	9.0914E-05	frozen
filter1	2.000	frozen
thcknss1	1.3340E-02	frozen
filter2	6.000	frozen
thcknss2	4.6609E-06	frozen
filter3	32.00	frozen
thcknss3	0.	frozen
filter4	48.00	frozen
thcknss4	6.8707E-05	frozen
filter5	19.00	frozen
thcknss5	1.0000E-05	frozen
filter6	45.00	frozen
thcknss6	0.	frozen
lineE1	1.550	-1.000
sigma1	8.0000E-03	frozen
norm1	8864.	-1.000
lineE2	1.486	-1.000
sigma2	4.3000E-04	frozen
norm2	3.5642E+05	0.5631E+05
norm	0.7449	0.8526E-03

Table 4.21: Fitting parameters for `ssd_x` white beam, all energies with  $133.4 \mu\text{m}$  Al filter. Runid 500627, channels = 21–49, 64–279, and 301–549, nbins = 494 reduced  $\chi^2 = 5.836680$

Parameter	Value	Status
alpha	0.	frozen
radius	2.500	frozen
distance	1.6242E+04	frozen
E_electr	798.7	frozen
H	1.491	frozen
e_to_cur	7.6970E-13	frozen
N_electr	0.	frozen
current	1.7721E+05	frozen
pileup	3.9025E-04	0.6484E-03
filter1	2.000	frozen
thcknss1	1.3340E-02	frozen
filter2	6.000	frozen
thcknss2	0.	frozen
filter3	32.00	frozen
thcknss3	4.0312E-05	0.3247E-05
filter4	48.00	frozen
thcknss4	1.2267E-06	0.2486
filter5	19.00	frozen
thcknss5	1.2500E-04	frozen
filter6	45.00	frozen
thcknss6	0.	frozen
lineE1	1.488	frozen
sigma1	4.3000E-04	frozen
norm1	8.3373E+07	frozen
lineE2	1.552	frozen
sigma2	8.0000E-03	frozen
norm2	8.3937E+04	frozen
norm	0.6670	0.8215E-01

Table 4.22: Fitting parameters for `ssd_x` white beam, higher energies with 133.44  $\mu\text{m}$  Al filter. Rumid 500483, channels = 189–589, nbins = 401 reduced  $\chi^2 = 1.232058$

Det.	File	ID	keV	raw	Pileup	$\sigma$	lost	e	Rate	ROIrate
		500+		QE%	Corr'd%	%	Hz		Hz	Hz
<code>ssd_5</code>	noal5.log	614	3.5–6.6	101.9	102.2	1.3	4.66	8	1782.83	45.6616
	noal5_2.log	615	3.5–6.6	98.2	98.3	0.6	0.695	5	1112.03	28.3543
	MEAN		3.5–6.6	98.99	<b>99.1</b>	<b>0.6</b>				
	thickal5.log	635	3.5–6.5	59.8		1.1				
	fatal5.log:	627	4.8–10.9	75.0		0.8				
<code>ssd_x</code>	noal_sx700.log	480	2.8–5.9	73.3	73.4	0.6	1.442	5	984.231	20.38
	noal_2_sx700.log	481	2.8–5.9	72.9	72.9	1.0	0.387	2	405.229	8.00589
	MEAN		2.8–5.9	73.17	<b>73.3</b>	<b>0.5</b>				
	thickal.log	470	3.2–9.8	67.7		0.3	15.28			
	fatal.log	483	3.8–10.6	66.7		8.2	2.153			
<code>ssd_5</code>	noal5_all.log	614	0.4–6.5	97.19		0.2				
	noal5_all_2.log	615	0.4–6.5	99.62		0.1				
	thickal5_all.log	635	0.4–6.0	55.31		0.1				
	fatal5_all.log	627	0.4–10.8	68.93		0.1				
<code>ssd_x</code>	noal_all_sx700.log	480	0.4–7.9	71.80		0.7				
	noal_all_2.log	481	0.4–7.9	83.33		0.2				
	thickal_all.log	470	0.8–5.9	60.60		0.1				
	fatal_all.log	483	0.4–11.6	74.49		0.04				

Table 4.23: Summary of white beam normalization runs. See text for explanation.

time in the input data file to correct for dead time by counting the pulser pulses in the pulser peak appearing in the pulse height spectrum and dividing by the recorded total number of pulses from the pulser. The sixth column gives the QE corrected for pulser pileup, which is not accounted for in our XSPEC/SYNCH model. This is a very small correction done by adding back the pulses that have piled up with the pulser pulses. These appear in the pulse height spectrum at channels just above the pulser peak. They are recorded in column eight. Column seven gives the estimated  $1\sigma$  error in “Pileup Corr’d.” Column nine gives the number of electrons in the storage ring for that run. Column ten gives the raw counting rate obtained by summing over all channels in the pulse height spectrum, and column ten gives the rate recorded in the ROI by the HXDS. This is just for the purpose of a sanity check for the four runs shown with no Al filter. It demonstrates that the rates are closely proportional to the number of electrons in the storage ring for runs 500614 and 500615, and also for runs 500480 and 500481. This seems to eliminate the possibility that the anomalous value of the QE for `ssd_x` could be a result of some gross error in the reduction and analysis of the pulse height data, because the raw rates show the same effect.

The rows with the entry MEAN give our best estimate of the overall QE and its  $\sigma$  for the two detectors. For `ssd_5` the result is consistent with 1.00. For `ssd_x` it is not. This discrepancy between the two detectors is not seen in the SX700 QE measurements. For example, in Tables 4.7 and 4.8 we see that the measured and predicted QE’s are in very good agreement with a model that just includes low energy absorption from the known windows in the detector. There is no overall discrepancy of 27% as there is in the white beam measurements for `ssd_x`. This agreement is also seen in the flat field calibration done at XRCF Zhao et al. (1998). We must therefore assume that the white beam calibration of `ssd_x` is flawed, and is to be disregarded. However, we are continuing to investigate this problem to see if we can identify what caused the problem, such as a misalignment or some other thing that may have blocked some of the beam from entering the

	-400	-200	0	200	400
400	...	44.44	43.58	40.63	...
200	40.49	46.05	43.10	43.79	41.67
0	44.31	42.08	44.49	41.88	44.77
-200	43.23	44.77	42.50	43.12	41.78
-400	...	41.79	41.92	43.41	...

Table 4.24: BESSY `ssd_x` uniformity scan; unprocessed `sum` file data Rates are in counts per second; coordinates are in  $\mu\text{m}$ .

detector aperture.

#### 4.6.5 Icing

Description of the detector and modeling of ice build up (we hope).  
Trends of ice build up as a function of time  
Nice plots again, etc.

#### 4.6.6 Detector Uniformity

A uniformity scan of the SSD's was done at BESSY as well as XRCF. The scan at BESSY was done on the white light beam line with a movable  $140 \mu\text{m}$  aperture. The aperture was scanned in a  $5 \times 5$  raster pattern on  $200 \mu\text{m}$  spacing. This gave a coverage of an area of about  $1 \text{ mm} \times 1 \text{ mm}$ . A similar scan was done at XRCF on the `ssd_x` detector using the focused HRMA beam.

The results from the BESSY `ssd_x` uniformity scan are shown in Table 4.24. These are unprocessed results based on the region of interest sums recorded in the `sum` files. No corrections for pileup, deadtime, or any other postprocessing effects have been made. The mean of these 21 measurements is 43.04 and the standard deviation is 1.43, or 3.3% of the mean. The number of counts in each measurement should be displayed, to see if these results are consistent with poisson fluctuations.

## 4.7 Future Work

- Continue to try to figure out why so many of the white beam runs give a low QE by 20–30%.
- Include recent fit with the new response matrices just built.
- More careful analysis of uniformity scans.
- Need to add more complete error propagation to BESSY results, to include effect of errors in measuring storage ring parameters.